

An explainable three dimension framework to uncover learning patterns: A unified look in variable sulci recognition

Michail Mamalakis^{1,2*}, Heloise de Vareilles¹, Atheer Al-Manea¹, Samantha C. Mitchell³, Ingrid Agartz⁶, Lynn Egeland Mørch-Johnsen^{4,5}, Jane Garrison³, Jon Simons³, Pietro Lio², John Suckling¹ and Graham Murray¹

¹*Department of Psychiatry, University of Cambridge, Cambridge, UK.

²Department of Computer Science and Technology, Computer Laboratory, University of Cambridge, Cambridge, UK.

³Department of Psychology, University of Cambridge, Cambridge, UK.

⁴Norment, Division of Mental Health and Addiction, Oslo University Hospital, Institute of Clinical Medicine,, University of Oslo, Oslo, Norway.

⁵Department of Psychiatry and Department of Clinical Research,, Østfold Hospital, Grålum, Norway.

⁶Department of Psychiatric Research,, Diakonhjemmet Hospital, Oslo, Norway.

*Corresponding author(s). E-mail(s): mm2703@cam.ac.uk;
Contributing authors: hd488@cam.ac.uk; aa2359@cam.ac.uk;
sm2596@cam.ac.uk; jrg60@cam.ac.uk; jss30@cam.ac.uk;
pl219@cam.ac.uk; js369@cam.ac.uk; gm285@cam.ac.uk;

Abstract

Explainable AI is crucial in medical imaging. In the challenging field of neuroscience, visual topics present a high level of complexity, particularly within three-dimensional space. The application of neuroscience,

which involves identifying brain sulcal features from MRI, faces significant hurdles due to varying annotation protocols among experts and the intricate three-dimension functionality of the brain. Consequently, traditional explainability approaches fall short in effectively validating and evaluating these networks. To address this, we first present a mathematical formulation delineating various categories of explanation needs across diverse computer vision tasks, categorized into self-explanatory, semi-explanatory, non-explanatory, and new-pattern learning applications based on the reliability of the validation protocol. With respect to this mathematical formulation, we propose a 3D explainability framework aimed at validating the outputs of deep learning networks in detecting the paracingulate sulcus—an essential brain anatomical feature. The framework integrates local 3D explanations, global explanations through dimensionality reduction, concatenated global explanations, and statistical shape features, unveiling new insights into pattern learning. We trained and tested two advanced 3D deep learning networks on the challenging TOP-OSLO dataset, significantly improving sulcus detection accuracy, particularly on the left hemisphere. During evaluation with diverse annotation protocols for this dataset, we highlighted the crucial role of an unbiased annotation process in achieving precise predictions and effective pattern learning within our proposed 3D framework. The proposed framework not only annotates the variable sulcus but also uncovers hidden AI knowledge, promising to advance our understanding of brain anatomy and function.

Keywords: XAI, sulcal pattern, paracingulate sulci, deep learning, brain classification

1 Introduction

In the realm of computer vision, the concern of explainability is significant across various domains, including natural scenes, climate, automotive, medical imaging, and neuroscience. We categorize these domains into self-explainable, semi-explainable, and non-explainable applications based on the stability of the validation protocol and the propensity to explore new patterns (Fig. 1,a).

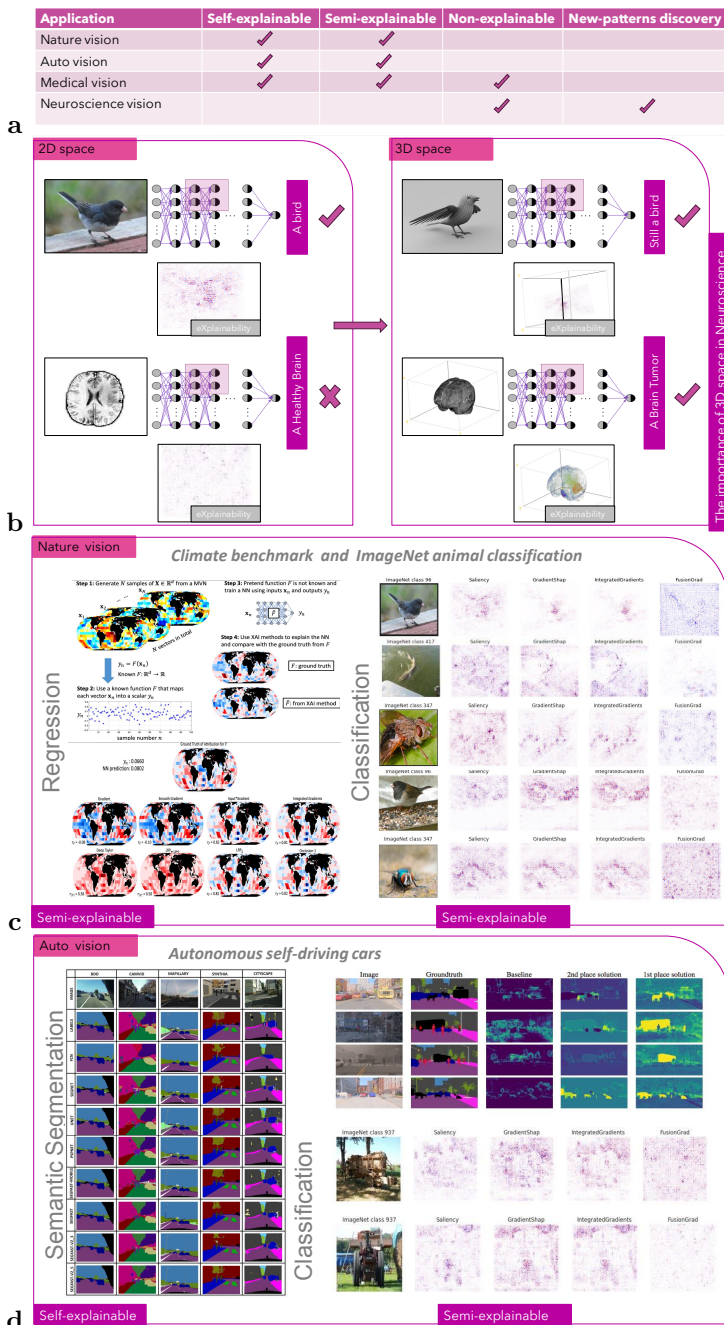
1. Self-explainable applications pertain to tasks where delving into the AI's internal mechanisms is unnecessary due to limited variability in the annotation protocol and the direct interpretability of AI predictions.
2. Semi-explainable applications have a more variable annotation protocol, requiring localized explanations within the AI pattern learning process to ensure effective training. This category demands partial interpretability to confirm the accuracy of the AI's training process.
3. Non-explainable AI applications are characterized by significant variance in the annotation protocol across different experts.

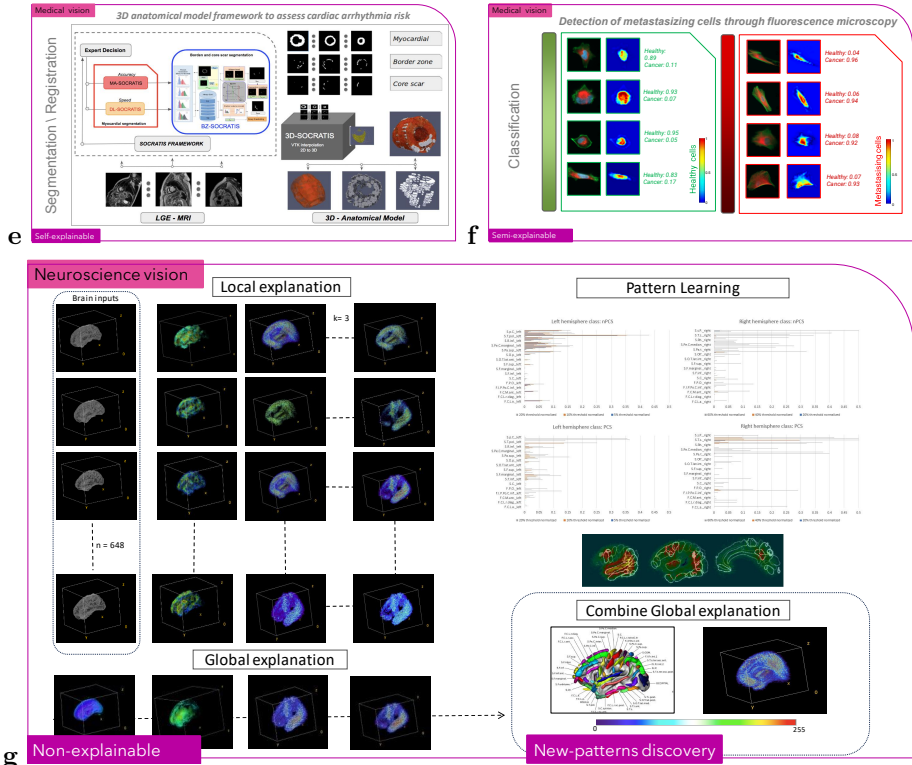
In natural computer vision, applications like animal classification and climate regression [1] necessitate local explainability (see Fig. 1,c). Automotive computer vision, which includes vehicle and object classification, as well as semantic segmentation for self-driving cars [2, 3] (Fig. 1,d), benefits from self-explainability, as it fosters human trust and understanding.

In medical image analysis, self-explainable applications cover tasks where inner workings of the AI are unnecessary to understand due to low variability in the annotation protocol and easily interpretable AI predictions, such as segmentation and registration [6, 7] (Fig. 1,e). Conversely, semi-explainable applications involve greater annotation protocol variability, necessitating localized explanations within the AI pattern learning process for proper training (e.g., classification in a well-established disease annotation protocol, [5], Fig. 1,f). Non-explainable AI applications show substantial variability in the annotation protocol across experts clinicians. Network pattern learning requires thorough investigation and validation using a combination of local and global eXplainable AI (XAI) methods. Even among experts, a knowledge gap exists, which AI can potentially address when validating fundamental protocol knowledge (e.g., classification in a non-established disease annotation protocol, [8], Fig. 1,g).

In neuroscience, a highly challenging field, vision-related topics exhibit high complexity, particularly concerning 3D space (Fig. 1,b). Ordinary 2D explainability and validation of local and global explanations through a single biased method fall short and even wrong (Fig. 1,b). Identifying new patterns and validating existing ones necessitates the use of our proposed 3D framework, surpassing traditional explainability approaches (Fig. 1a,e,f,g). For example, the folding of the human brain, established during gestation, is generally consistent among individuals. Post-natal development will affect sulcal metrics but the pattern of sulcation established at birth remains stable throughout life, preserving crucial prenatal neurodevelopmental information [9]. Detecting and annotating sulcal features from brain MRI is hindered by inter-individual variability in sulcation, making manual annotation time-consuming and subjective, therefore impeding efficient use of extensive open-access MRI databases. While automated methods excel in primary sulci detection, the variable shape and presence/absence of secondary sulci present a more complex computational hurdle [10]. Successful automation through generalized, unbiased annotation would aid studies on brain folding variations which depict critical developmental periods and may relate to cognitive, behavioral, and developmental studies, along with psychiatric and neurological disorders. Brain folding is linked to brain function, and specific folding patterns correlate with susceptibility to neurological issues [11]. For instance, the paracingulate sulcus, a variable secondary sulcus, is associated with cognitive performance and hallucinations in schizophrenia [12],[13],[14],[15]. Training networks to recognize its presence or absence in structural MRI allows for assessment of its functional relevance and impact on critical functions like reality monitoring in larger datasets [16].

Fig. 1: Different computer vision tasks and the importance of the proposed 3D eXplainable Artificial Intelligence framework.





a, The table presents the importance of explainability in computer vision across different domains: natural scenes, automotive, medical imaging, and neuroscience. We categorize them based on validation protocol stability and pattern exploration. Self-explainable applications have easily interpretable AI predictions and a stable annotation protocol. Semi-explainable applications require localized explanations for effective AI network training due to a variable annotation protocol. Non-explainable AI applications show significant variability in the annotation protocol among experts. **b**, The importance of three dimensional space in computer vision task in neuroscience compare to nature and traditional computer vision classification tasks. **c**, The nature vision with different applications of animal classification (right, semi-explainable) and climate regression (left, semi-explainable, figures are adapted from [1]). In both field local explainability is just needed (local: explanation of a specific sample of the dataset). **d**, The automotive vision with different applications of vehicles classification (right, semi-explainable) and semantic segmentation for automatic self-driving cars (left, self-explainable, figures are adapted from [2, 3]). **e**, Medical vision and self-explainable application in cardiac segmentation and registration (figures adapted from [4]) **f**, Medical vision and semi-explainable application in metastatic cell classification (figures adapted from [5]). **g**, Neuroscience vision and the need for local, global, combined global, and new-pattern learning identification in non-explainable classification. It highlights the necessity for a 3D structural space (local: specific dataset sample explanation; global: all dataset sample explanation).

In this study, we introduce a mathematical formulation that classifies distinct explanation requirements across varied computer vision tasks, encompassing self-explainable, semi-explainable, non-explainable, and new-pattern learning applications. Based on this classifications we present a 3D explainability framework (Fig. 4c.) designed to validate the learned patterns within a deep learning network engaged in a binary classification of presence or absence of the paracingulate sulcus. Additionally, our explainability framework unveils sub-regions associated with the presence or absence of this variable sulcus. Two distinct local explainability methods (GradCam and SHAP) were developed in 3D space and concatenated with an interpretable dimensionality reduction technique. This combination aimed to generalize outcomes and reveal the learning patterns followed by the networks. For the prediction of the paracingulate sulcus presence, two different 3D deep learning networks were employed: a straightforward deep 3D convolutional neural network (simple-3D-CNN), and a two-headed attention layer network with variations in backbone options (2CNN-3D-MHL and simple-3D-MHL). The networks utilized 3D brain inputs obtained through preprocessing of structural MRI scans, comprising two distinct modalities: the grey-white surface and the sulcal skeleton from both the right and left hemispheres. To train, validate and test our deep learning networks, we used a comprehensively annotated cohort of 596 subjects from the TOP-OSLO study [17]. The dataset was partitioned into distinct sets for training (70%), validation (20%), and testing (10%) purposes.

Our proposed 3D explainability framework provides both localized and global explanations alongside classification outcomes, allowing the identification of decision-relevant sub-regions through a post-fusion transformation of explanatory and statistical features. This novel technique detects a variable sulcal pattern, facilitating its extensive exploration in cognitive and neurological studies. It also highlights the importance of utilizing an unbiased and well-established annotation protocol in hypothesis-driven computer vision tasks.

2 Related work

2.1 The application: Sulcal pattern studies

Cortical folding, which almost entirely develops in-utero, results in an inter-individual variability that is eschewed in populational studies. Yet, focusing on the variability of sulcal pattern can be motivated by different reasons: strict descriptive anatomy, refinement of inter-subject registration, investigation of mechanisms at play during neurodevelopment, and search for anatomo-functional correlates. Links to brain function can also be addressed to either investigate healthy functional variability (e.g. cingulate folding pattern and functional connectivity), [18]), or relationships between cortical folding pattern and pathological outcomes (e.g. paracingulate folding and hallucinations in schizophrenia [19]). The study of cortical folding variability can be addressed through global methods, with whole brain or regional considerations of generic

sulcal parameters (e.g. gyrification index or sulcal pits), but refined investigations of sulcal patterns require the capability for a focus on specific sulci, hence the need for automated sulcal recognition methods. A number of different methods have been developed for automated sulcal labelling in a general setting (for review, see [20]). Yet, to the best of our knowledge, no method is currently implemented to automatically label the paracingulate sulcus in a 3 dimensional approach (a 2 dimensional approach for a specific MRI slice has been proposed [21]). The fact that the paracingulate sulcus is omitted general brain labelling is probably due to the way in which it is anatomically specified: it is not only defined by its location in the brain but also by its orientation (parallel to the cingulate sulcus). Hence, even newer sulcal labelling implementations do not identify within the folding of the medial frontal cortex [10]. Nevertheless, investigating the whole-brain anatomical correlates of sulcal variability incurred by the presence of the paracingulate sulcus is potentially important to understand some of the common and severe psychotic symptoms. Automatic detection of the paracingulate sulcus is in itself useful for large dataset exploration, especially since it has previously been related to functional variability in reality monitoring [16]. Additionally and unprecedentedly, adding an explainability component allows us to interrogate the anatomical covariates of the paracingulate sulcus gaining a broader vision on the mechanisms at which it may have a role.

The automated labelling of sulci allow shape analysis and pattern investigation of specific sulci on large datasets. These analyses can be led using different methods, on which the following are a general overview. First, simple metrics can be extracted automatically using the BrainVISA software [22], such as the length or mean depth [23]. Similarly, the local gyrification index can be derived from these automatically extracted metrics, defined as the ratio between a sulcus's surface area and the outer cortical area [24]. Yet, these metrics provide limited information on sulcal pattern. Automated methods providing more advanced sulcal pattern characterization have been proposed, as, for example, the comparison of positioning of the superior temporal sulcus between two cohorts [25]. Another way of investigating sulcal pattern is by automatically capturing shape features. This can be done by looking for a predefined shape feature, such as a characteristic bulk in a sulcus [26] or a sulcus's depth profile [27]. Alternatively, this can also be investigated by using machine learning to automatically extract shape features from either a sulcus or a group of sulci [28–31], with no prior expectation on the shape feature to capture. In addition to offering methodologies for investigating sulcal shape variability, these studies highlight our limited current understanding of the implications of sulcal pattern variability.

2.2 Explainable methods

There has been a notable surge in recent publications concerning eXplainable Artificial Intelligence (XAI) and machine learning (XML) in the field of medical

image analysis and neuroimaging [32],[33],[34],[6]. XAI can be broadly classified into two methodological approaches: transparent and posthoc. On the one hand, transparent methods primarily focus on models that exhibit properties such as simulatability, decomposability, and transparency. These methods are closely associated with linear techniques such as Bayesian classifiers, support vector machines, decision trees, and K nearest neighbor algorithms [35]. On the other hand, posthoc methods are often utilized in conjunction with AI techniques that aim to uncover nonlinear mappings within complex datasets. One commonly employed technique is local interpretable model-agnostic explanations (LIME), which assesses the robustness of explanations by introducing noise and perturbations to the dataset [36]. Posthoc techniques encompass approaches that specifically address the nonlinear behavior of both the model and the dataset, making them a comprehensive collection of model-specific and model-agnostic techniques [32, 35]. In the realm of computer vision, model-agnostic techniques such as LIME, perturbation, and layer-wise relevance propagation (LRP) find extensive applicability [37]. In opposition, model-specific techniques include methodologies like feature relevance, condition-based explanation, and rule-based learning [35, 38]. In the context of medical imaging, explainable methods primarily revolve around attribution and perturbation techniques [39]. Attribution techniques assign weight definitions to features within the network for each layer (e.g., LIME, LRP, GRAD-CAM, SHAP) [39], whereas perturbation techniques primarily focus on manipulating input data with respect to the predictions of machine learning (ML) or deep learning (DL) techniques [36]. Additionally, the Occlusion technique is another important approach that explores the significance of latent features to the model [36, 39]. Among the various explainable methods in medical imaging, the GRAD-CAM method stands out as the most frequently employed [36].

In line with the growing trend of utilizing and sharing existing data, it is essential to investigate "hybrid models" that combine AI approaches with biologically driven models [40]. This raises the question of whether AI converges towards the expected solution. Specifically, explainable AI applied to neuroscience and neurostimulation encounters the challenge of the "curse of dimensionality" due to the high-dimensional nature of imaging data. Consequently, this challenge highlights the necessity of considering simpler models and incorporating variable selection techniques. While this example primarily pertains to technical and computational issues, it is crucial to address past clinical failures as well [40]. Furthermore, explainability in AI has several valuable implications. It can foster trust in algorithms, aid in understanding risk and side effects, assist in identifying therapeutic targets, provide insights into the progression of disease and response to treatments, support decision-making, enable closed-loop control, and contribute to the design of safety parameters for FDA-regulated therapies. While explainability has the potential to enhance trustworthiness, transparency, and fairness, it is important to distinguish and acknowledge that they are distinct but interconnected concepts. The readiness

of scientists and healthcare professionals to accept the validity and reliability of machine learning results, even without comprehensive knowledge of how the results were derived, is closely related to trustworthiness. Trust relies on five key factors: the quality of the data, the reliability of the system, the integrity of the workflow, the accuracy of the outputs, and the ability to effectively communicate the algorithm's results [40].

In our study, we present a mathematical formulation delineating various categories of explanation needs across diverse computer vision tasks. We have developed a unique 3D explainability framework targeting the validation of deep learning networks' ability to learn patterns within binary classification tasks relevant to neuroscience. This framework integrates local explanations (an implementation of state-of-the-art GradCam and SHAP methods in 3D space), global explanations via dimensionality reduction, and concatenated global explanations with statistical 3D shape features. Through this approach, novel insights into pattern learning are unveiled, amplifying the credibility and reliability of deep learning networks. Notably, our framework effectively identifies significant sub-regions by merging explainable and statistical features from the evaluation dataset.

3 Methods and Background

3.1 Mathematical formulation of the problem

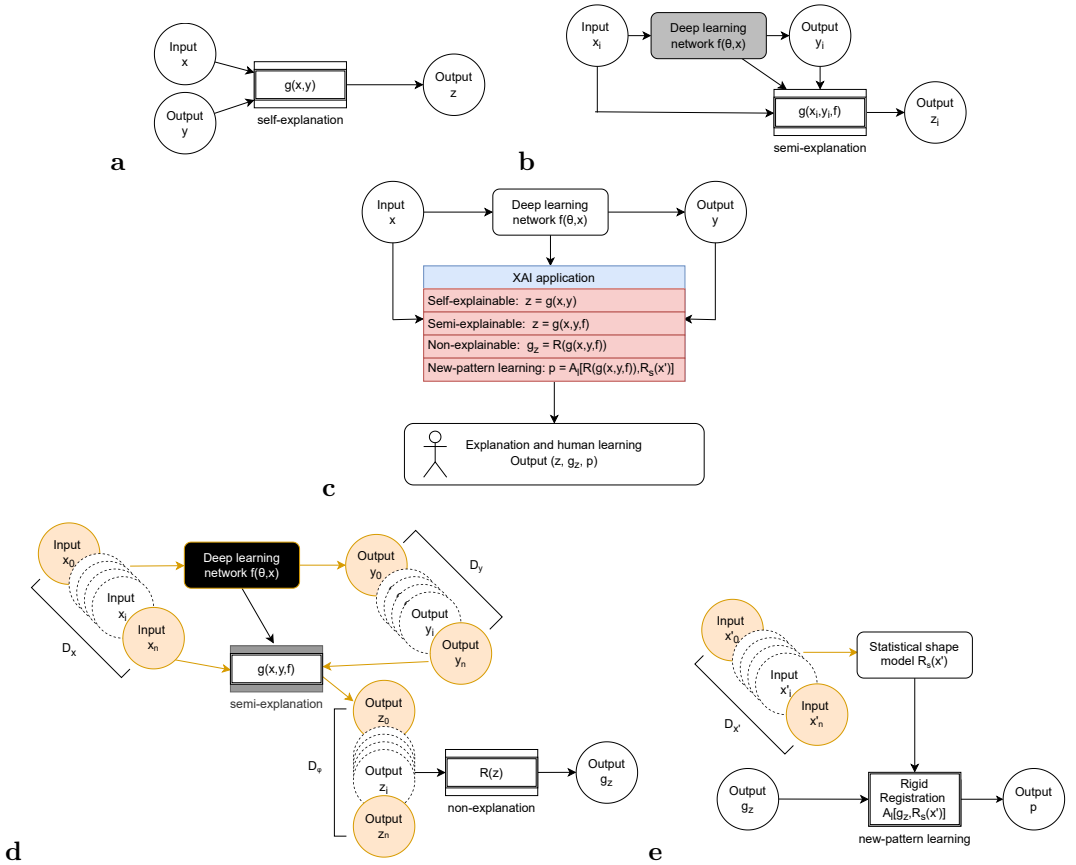
For an input $\mathbf{x} \in R^d$, we define a deep learning model function $f(\mathbf{x}; \theta)$ with $f : R^d \rightarrow R^c$, where c is the output dimension, d is the input dimension and θ consists of the parameters of the model in a computer vision problem (e.g., for a classification task c is the number of classes, and for a segmentation task $c \leq d$). The inference of the model is denoted as $y = f(\mathbf{x}; \theta)$ where $\mathbf{y} \in R^c$ is the predicted probability of the corresponding dimension c (Fig. 2c.). An explanation method g from a post-hoc family of explanation methods G takes as inputs the f , \mathbf{x} and \mathbf{y} and returns an explanation map \mathbf{z} . The $G(\mathbf{x}, \mathbf{y}, f)$ contains multiple explanation methods, denoted as g^j where j is the index of each post-hoc method. The explanation map of each input \mathbf{x} can be given by $z = g(\mathbf{x}, \mathbf{y}, f)$ where $\mathbf{z} \in R^d$ and has the same dimension space as the input \mathbf{x} . For computer vision applications, we define $D : \mathbb{R}^d \times \mathbb{R}^c \times \mathbb{R}^d \mapsto \mathbb{R}_{\geq 0}$ as a tuple of datasets $D = (\mathbf{x}_i, \mathbf{y}_i, \mathbf{z}_i)_{i=1}^n$, that denotes input-output-explanations triples, where n is the total number of the validation examples. D_x denotes all \mathbf{x}_i , D_y denotes all \mathbf{y}_i and D_z denotes all \mathbf{z}_i in D . In this study, we define as "global explanation" a map g_z that represents all the local explanations for the whole validation dataset D_z . The global explanation can be viewed as a dimensionality reduction function $g_z = R(\mathbf{z})$ of the whole local explanations D_z (for example, in a setting of a principal component analysis, g_z would correspond to the eigenvectors). We define four distinct applications of explainability needs: self-explainable, semi-explainable, non-explainable, and new-pattern learning (Fig. 2c.).

The mathematical representation of the self-explainable application involves an interpretable function $g(\mathbf{x}, \mathbf{y})$ that solely employs the inputs \mathbf{x} and outputs \mathbf{y} of the deep learning model f . Given a clear validation protocol and sufficient correlation between the inputs and outputs of the deep learning network, there is no necessity for explaining the hidden parameters of the network. Therefore, this application can be named as a '*white application*' (Fig. 2a,). The mathematical description of the semi-explainable application comprises a set of explanation methods $g(\mathbf{x}, \mathbf{y}, f)$ that utilize both the inputs \mathbf{x} and outputs \mathbf{y} , along with the hidden parameters of the deep learning model $f(\mathbf{x}; \theta)$. Due to a more variable annotation within the validation protocol and insufficient correlation between the inputs and outputs of the deep learning network, a sub-group $S_D = (\mathbf{x}_i, \mathbf{y}_i, \mathbf{z}_i)_{i=1}^o$ of local explanations \mathbf{z} of the hidden parameters are needed (where o represents a fixed number of samples from the validation dataset D , $S_D \subset D$ and $o < n$). Consequently, this application can be named as a '*grey application*' (Fig. 2b,).

The mathematical representation of non-explainable application involves a set of explanation methods $g(\mathbf{x}, \mathbf{y}, f)$ that relies on the inputs \mathbf{x} and outputs \mathbf{y} in addition to the hidden parameters of the deep learning model $f(\mathbf{x}; \theta)$. With significant variance in annotations within the validation protocol and differences in ground truth extractions across various experts, the correlation between the inputs and outputs of the deep learning network is inadequate. Thus, there is a requirement for global explanations g_z , by using the whole validation dataset $D = (\mathbf{x}_i, \mathbf{y}_i, \mathbf{z}_i)_{i=1}^n$ (where n encompasses the total number of samples from the validation dataset D). This application can be named as a '*black application*' (Fig. 2d,). In the new-pattern learning application a collection of potentially significant markers can be computed for the initial computer vision task by align the global explanations g_z with a statistical shape model $R_S(\mathbf{x}')$. The statistical model is generated by inputs \mathbf{x}' of a super dataset $D_{x'}$ of the validation dataset D_x ($D_x \subseteq D_{x'}$). This model tries to capture the generalized features of interest and the generalized shape related with the computer vision task (in our case multi-atlas of the brain). The statistical shape inference is given by $r_{\mathbf{x}'} = R_S(\mathbf{x}')$ where $r_{\mathbf{x}'}$ is the output statistical shape that describes the $D_{x'}$ dataset. The alignment can be done by a rigid registration function $A_l(g_z, r_{\mathbf{x}'})$ of the $r_{\mathbf{x}'}$ and the g_z (Fig. 2e,).

In our application, we developed a novel 3D framework for the non-explainable and new-patterns learning tasks (Fig. 2d,e,). Specifically, we utilized two distinct explanation methods, denoted as g^1 and g^2 , belonging to the post-hoc family G (SHAP and GradCam), expanded in three-dimensional space. We concatenate the outcomes obtained from the two explainable methods with the results derived from a statistical feature extraction model. The statistical model was a transparent dimensionality reduction algorithm applied to the input data \mathbf{x} of the validation cohort D_x . This whole approach was intended to mitigate any potential biases and enhance the robustness of the pattern learning discovery.

Fig. 2: A mathematical formulation of the explainability need in different deep learning applications.



a, Self-explainable application utilises methods $g(x, y)$ focusing solely on the inputs x and outputs y of the deep learning model f . With a clear validation protocol and strong input-output correlation, explaining the hidden parameters becomes unnecessary. **b**, Semi-explainable application employs methods $g(x, y, f)$ integrating inputs x , outputs y' , and the hidden parameters of $f(\theta, x)$. Due to varied annotation and insufficient input-output correlation, local explanations for specific samples in the validation dataset D become necessary. **c**, The mathematical representation presents the overall XAI framework for a specific method g across different explainability applications. **d**, Non-explainable application involves methods $g(x, y, f)$ relying on inputs x , outputs y , and the hidden parameters of $f(\theta, x)$. Due to significant variance in annotations and discrepancies in ground truth extractions, a necessity arises for global explanations g_z using the entire dataset $D = (x_i, y_i, z_i)_{i=1}^n$. **e**, In the new-pattern learning application, crucial markers for the initial computer vision task are derived by aligning global explanations g_z with a statistical shape model $R(x')$ generated from a supergroup $D_{x'}$ describing the classification application's overall shape. A rigid registration function $A_l(g_z, r_{x'})$ is used to align the output of the statistical shape model with the global explanations.

3.2 Architectural design of deep learning networks for the classification task

The initial deep learning model was a 3D Convolutional Neural Network (CNN) with five levels. Each level incorporated a CNN block with a 3D convolution layer, a 3D max-pooling layer, and a batch normalization layer. In the first three levels, the 3D convolution layer employed 64, 128, and 256 filters, respectively (as shown in Fig. 3a.). The last level connected to a multi-layer perceptron (MLP) for the final prediction (as illustrated in Fig. 3a.). The MLP comprised three distinct perceptrons and two dropout layers to estimate epistemic uncertainty.

For the second network (Fig. 3b.), we used a combination of multi-head attention layers (MHL) to focus on the global diversity and variation of a backbone output. To reduced the biased choice of only one backbone selection, we opted for two distinct backbone networks: (i) a 3D Convolution layer block with two level of 64 and 128 filters a Global Average Pooling, and a perceptron of 32400 hidden layers (2CNN-3D-MHL), and (ii) the straightforward 3D CNN network outlined previously. (Fig. 3b., simple-3D-MHL). We used the multi-head attention mechanism described in [41] and as we used a two-head attention of the same input, we called this approach "self-attention". The two heads ($head_c$) are given by:

$$head_c = AT(QW_c^Q, KW_c^K, VW_c^V) \quad (1)$$

where c is the backbone output. There are two outputs as we used the backbone twice, and each output is connected to a perceptron with N hidden layers (where N is equal to the product of the weight and height of the input image). The AT is the attention layer and it computed by:

$$AT(Q, K, V) = softmax\left(\frac{QK^T}{\sqrt{d_k}}\right)V \quad (2)$$

where the input matrix are combination of queries and keys of dimension d_k , and values of dimension d_v . Queries are packed together into matrix Q . The keys and values are also packed together into matrices K and V . The output of the MHL network is given from:

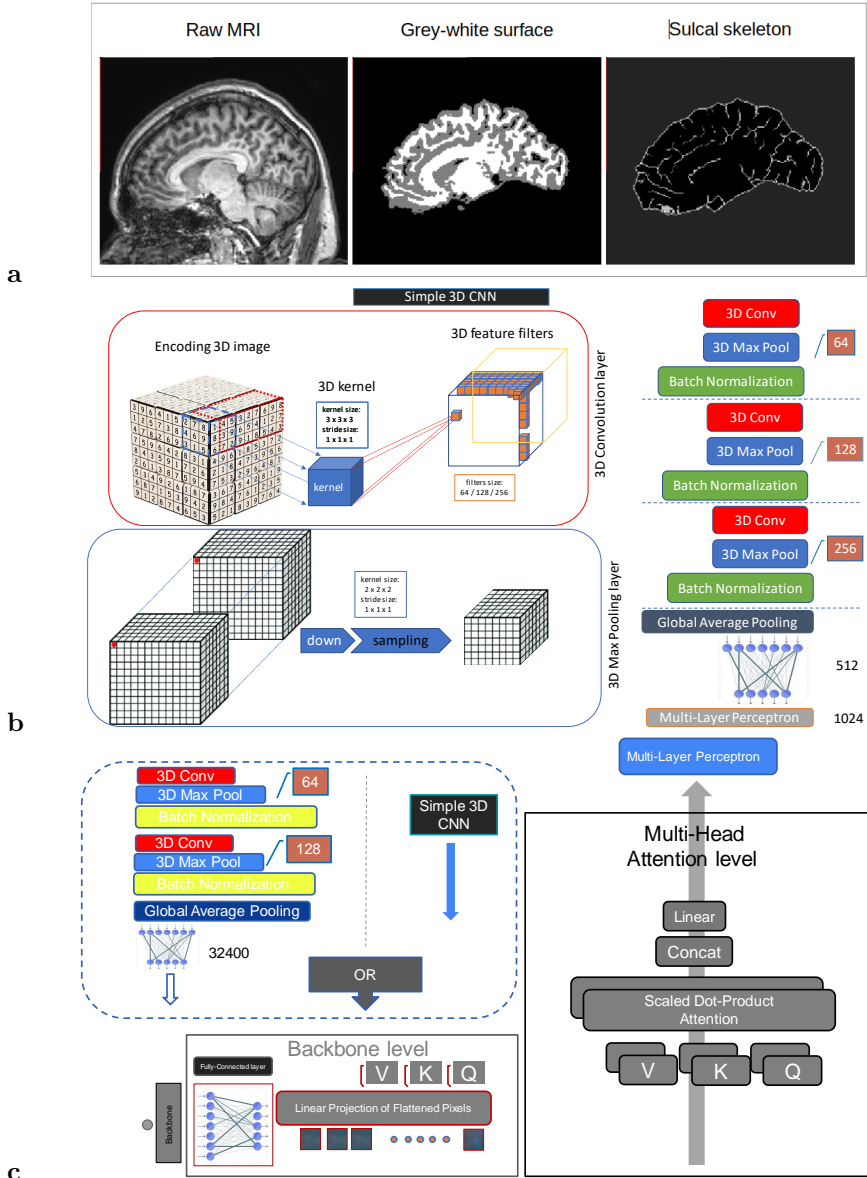
$$MHL = Concat(head_c, head_c) \quad (3)$$

where c defines by the $backbone_{output}$. The output of the MHL was passed again from the MLP presented above to make the final prediction.

3.3 Extending explainability methods in 3D space

Interpretability and explainability stand as crucial components within a classification study, serving to validate the accurate training of machine learning networks. Within this study, we employed two distinct explainable techniques:

Fig. 3: Illustration of the input modalities and the architecture of simple-3D-CNN and the simple-3D-MHL networks.



a-c, Illustration of the input modalities illustrated on a right hemisphere coronal slice. The highlight of the architectures of simple-3D-CNN and the three dimension MHL network. **a,** Input modalities illustrated on a right hemisphere coronal slice. More analytically the raw MRI of a given subject, the corresponding grey-white surface, and the corresponding sulcal skeleton. **b,** The architecture of simple-3D-CNN network with explanation of 3D Convolution layer (3D Conv) and 3D Max Pooling layer on the left. **c,** The three dimension MHL model with two different backbone choices, the full simple-3D-CNN (simple-3D-MHL) and the two level simple-3D-CNN layer (2CNN-3D-MHL).

the widely-utilized sensitivity local explainability technique in medical imaging applications known as the GradCam method [35], and a robust attribution explainability technique called SHAP [42].

Previously emphasized is the significance of the three-dimensional space in neuroscience applications. Consequently, there arises a necessity to extend the conventional 2D methodologies of GradCam and SHAP into the realm of three dimensions. In the pursuit of computing the class-discriminative localization map encompassing width w , height h , and depth d within a specific 3D brain MR image corresponding to a class c (PCS or nPCS), the computation involves determining the gradient of the score for class c , denoted as y^c , in relation to the o^{th} feature activation map (A^o) of the final convolution layer in each deep network. To determine the importance weights (α_o^c) for each o feature activation map, global average pooling is employed over the width (i), height (j), and depth (k) of each feature.

$$\alpha_o^c = \frac{1}{Z} \sum_i \sum_j \sum_k \frac{dy^c}{dA_{ijk}^o} \quad (4)$$

where Z the summation of i , j and k . Moreover, we used a weighted combination of forward activation maps and a *ReLU* to deliver the final GradCam activation map.

$$GradCam = ReLU\left(\sum_o \alpha_o^c A_{ijk}^o\right) \quad (5)$$

SHAP (SHapley Additive exPlanations, [42]) computes the attribution of each pixel of an input image for a specific prediction of a computer vision task. The attribution explainability methods follow the definition of additive feature attribution mainly as a linear function of:

$$g(f, x) = \phi_0 + \sum_{i=1}^M \phi_i x_i \quad (6)$$

where f is the prediction network, $g(f, x)$ is the explanation model, ϕ_i is the importance of each feature attribution ($\phi_i \in \mathbb{R}$), and M is the number of simplified input features (pixels). Shapley value estimation is one of the main mathematical formulations that the SHAP algorithm used to assign an importance value to each feature, representing the effect on the model prediction of including that feature (attribution). If we define a subset S of the total feature space (F) of an input 3D image I ($i = 1 \dots N$, where N is the number of samples in the dataset), and x_i is a 3D matrix of width w and height h and depth d for the i^{th} sample, and x_S is the subset of chosen features in the 3D space, then:

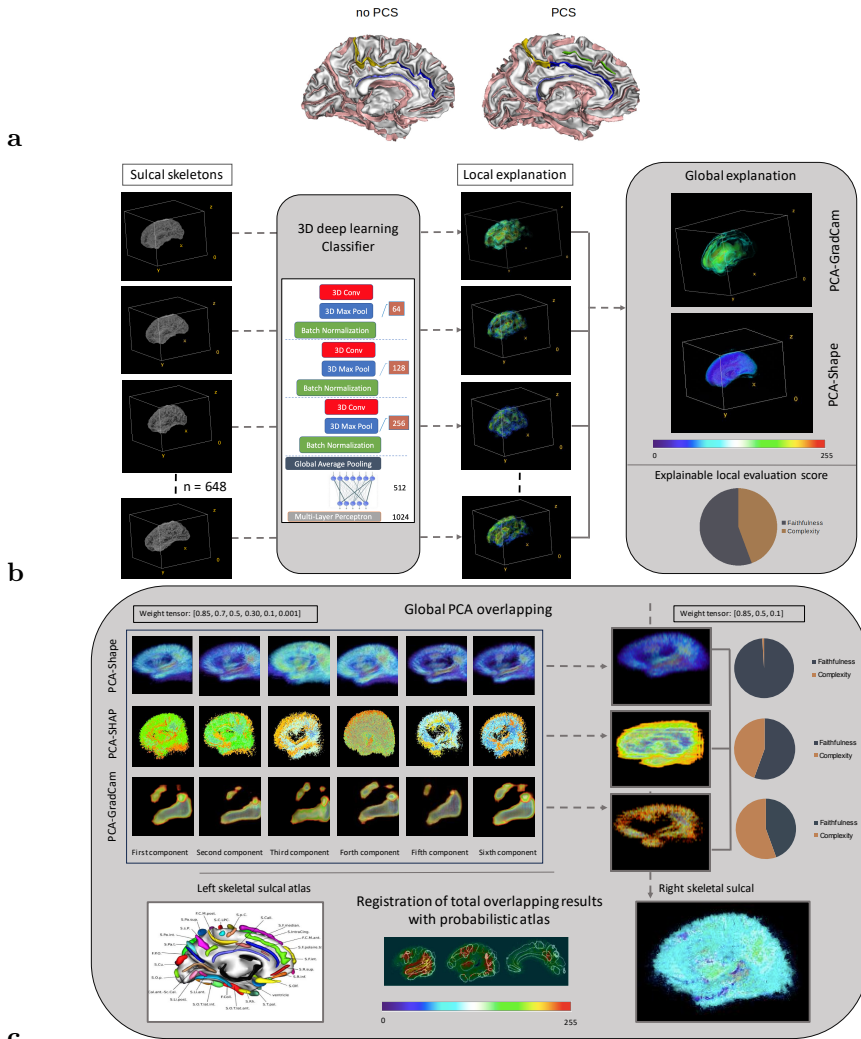
$$\phi_i = \sum_{S/(i)} \frac{S!(F-S-1)!}{F!} [f_{S(i)}(x_{S(i)}) - f_S(x_S)] \quad (7)$$

Here, $f_{S(i)}$ is a model trained with the presented x_s features, and f_S is another model trained with the features withheld. For our study, we used Deep SHAP [42] to describe our deep learning network models. In this approach, we used a chain rule and linear approximation as described in [42]. Using only local explainability techniques can introduce bias, so we aimed to mitigate this effect by applying an interpretable linear dimensionality reduction method: principal component analysis (PCA). We employed PCA to investigate the variability and generalization of both the GradCam (PCA-GradCam) and SHAP (PCA-SHAP) results and the two different input modalities images (PCA-Shape, for either sulcal skeleton or grey/white surface) from the total cohort (596 subjects), in order to assess the learning patterns of the deep learning network. The PCA was a six component analysis in 3D space.

3.4 The 3D explainable framework

In this subsection, we provide a detailed explanation of the technical aspects of the 3D explainable framework. Our objective was to unravel the learned patterns of the network and discern how an AI system discerns information across various 3D models, employing a transparent 3D framework. Fig. 4 c. illustrates the outline of the framework. We initiated the process by utilizing 3D brain inputs derived from preprocessing 3D structural MRI scans. This was done for the primary objective of distinguishing the existence or nonexistence of the paracingulate sulcus, separately within the left and right hemispheres. To do so, we deployed two distinct Convolutional Neural Network (CNN) architectures, namely simple-3D-CNN, and simple-3D-MHL. After classification, our focus shifted towards unraveling the inner workings of these networks and identifying the main features leading to the predictions. To do so, we used explanation techniques including sensitivity analysis, using the developed 3D GradCam, and feature attribution, through the developed 3D SHAP. These methods not only spotlight the areas of focus within the network but also highlight the components contributing to the predictive outcomes. To capture the main resulting features, we applied a Principal Component Analysis (PCA). This summarizes the explanatory outcomes, referred to as PCA-GradCam and PCA-SHAP.

Concurrently, we assigned scores to evaluate the quality of the explanations, ensuring their effectiveness reaches an acceptable threshold. To go further, we applied PCA to the input datasets to derive statistical features, denoted as PCA-Shape. Lastly, a mathematical formulation using overlap voting was applied, to identify the regions of interest originating from various PCA components derived from explanation methods and statistical features. Observing these overlapping regions allowed us to identify the features that primarily influenced each decision.

Fig. 4: Classification task determination and the proposed 3D explainable framework.

a, Illustration of the no paracingulate sulcus condition (no PCS), and the paracingulate sulcus condition (PCS, in green line) on two left hemispheres 3D white matter reconstructions obtained with BrainVISA. The cingulate sulcus is coloured in yellow and blue and the callosal sulcus is coloured in purple.

b, The 3D explainable framework that provides both local and global interpretations and explanations of our deep learning 3D classification network's results. The ratio of the faithfulness and complexity metrics are compute in that stage. In this example we include only the GradCam explainability method just for simplicity. **c**, A weighted averaging (Weight tensor: $[0.85, 0.7, 0.5, 0.3, 0.1, 0.001]$) of six PCA components produces the Global PCA image for PCA-Shape, PCA-GradCam, and PCA-SHAP. Following this, a weighted averaging (Weight tensor: $[0.85, 0.5, 0.1]$) of the three Global PCA overlapping images extracts the total overlapping image. This total overlapping image is then registered on a sulcal probabilistic atlas to unveil the model's pattern for determining the presence or absence of the paracingulate sulcus.

3.5 Pattern learning feature extraction through post-fusion overlapping explanations

To deliver global explanations and statistical features we analysed the results from the total datasets in terms of the GradCam and SHAP explanation methodologies using a principal component analysis (PCA) of a total of six components. The six-component analysis was selected as the optimal choice following a manual evaluation of configurations involving five, six, seven, and eight components. This selection was based on considerations of both time consumption and accuracy. These components were generated through the analysis of skeleton sulcal inputs and grey/white surface inputs of the total TOP-OSLO cohort, considering both the right and left hemispheres. Our purpose was to identify the attributes most relevant to these explanations, in order to observe the learning pattern associated with determining the presence or absence of the paracingulate sulcus.

To achieve this, we use voting weighting averaging, individually applied to each of the previous PCA components. The formulation is defined as follows:

$$G(X, W) = \frac{\sum w_i x_i}{\sum w_i} \quad (8)$$

where W is the weight tensor and the X is the pixel images tensor. The weight value within the weight tensor associated with each image is bounded within the range of 0.0 to 1.0. Our specific implementation used a weight tensor characterized by six diminished components: [0.85, 0.7, 0.5, 0.30, 0.1, 0.001], to facilitate a global PCA overlapping pattern learning. For the purpose of extracting a total overlapping pattern learning of each deep learning network we utilized the eq. 8 in the three global PCA pattern learning results (PCA-Shape, PCA-SHAP, PCA-GradCam), and a three-component weight tensor was deployed respectively: [0.85, 0.5, 0.1]. The three component weight tensor was determined as we emphasize more in the statistical features and the explainable method with the best performance in the complexity and faithfulness metrics (SHAP). To mitigate the potential bias that may arise from focusing on only one deep learning network we applied this approach to both the simple-3D-CNN and simple-3D-MHL networks. We identify the most relevant features for each classification class for both hemispheres. The identification of these features grants us insights into the mechanics underpinning the network's decision-making process. For enhanced clarity, the principal brain sub-regions of interest corresponding to the skeleton sulcal and white/gray surface are visually depicted in Fig. 3a,. Finally, the total overlapping images are then registered on a sulcal probabilistic atlas to unveil the model's pattern for determining the presence or absence of the paracingulate sulcus. The registration process involved affine transformations, encompassing translation, rotation, scaling, and geometry shrinking, to align with the probabilistic atlas.

4 Experiments

4.1 Cohort’s description and pre-processing image analysis

We used the structural MRI of 596 participants from the TOP-OSLO study [17] for a binary classification task. The participants encompassed individuals within the unaffected control spectrum (262), those within the schizophrenia spectrum (183), and those within the bipolar disorder spectrum (151). The participants were imaged using a 1.5 T Siemens Magnetom Sonata scanner (Siemens Medical Solutions, Erlangen, Germany). The modality used was T1-weighted structural MRI, and the input files consisted of DICOM images. Two experts, A.A. and H.V., performed image annotations, categorizing them into two classes: ‘no paracingulate sulcus’ (nPCS) and ‘paracingulate sulcus’ (PCS). This annotation was based on the protocol described in [43], with further details available in the supplementary materials under ‘PCS classification,’ and it is illustrated in Fig. 4. Image analysis techniques were applied to all slices to reduce artefacts. We used noise filters such as binomial deconvolution, Landweber deconvolution [44], and curvature anisotropic diffusion image filters [45] to reduce noise in the images.

4.2 Processing of two distinct input modalities

We initially processed the brain structural MRIs using the BrainVISA software [22] and extracted two different modalities for our input: the grey-white surface and the sulcal skeleton. These were extracted from the raw MRI from a succession of bias correction, histogram analysis, brain segmentation, hemisphere separation, dichotomization of the white matter from the union of grey matter and cerebrospinal fluid, and skeletonization of the result, as detailed in [46]. Specifically, the grey/white boundary was obtained by minimizing a Markov field and the segmentation used homotopic deformations of the hemisphere bounding box, resulting in the grey-white surface, where voxels are dichotomised into either grey or white. The skeleton was then derived from this object by applying a homotopic erosion embedding a watershed algorithm, that preserves the initial topology, resulting in the sulcal skeleton. These two modalities were then used to train and evaluate our networks as well as our explainability methods. Fig. 3a,b,c. show the structural MRI and the corresponding grey-white surface and sulcal skeleton outputs from BrainVISA.

4.3 Hyper-parameters initialization

After randomly shuffling the data, each dataset was split into training, validation, and testing sets containing 70%, 20%, and 10% of the total number of images, respectively. Sparse categorical cross-entropy was used as the cost function and the loss function was optimized using the Adam algorithm [47]. The learning rate was exponentially decreased during the first 50 epochs and then fixed at 0.0001 for the last 50 epochs. To train the networks, an early

stopping criterion of 10 consecutive epochs was employed and a maximum of 100 epochs was used for all input modalities (sulcal skeleton and grey/white matter) for both the left (L) and right (R) hemispheres. Finally, we use data augmentation techniques including rotation (around the center of the image by a random angle from the range $[-15^\circ, 15^\circ]$), width shift (up to 20 pixels), height shift (up to 20 pixels), and ZCA whitening (add noise in each image) to avoid overfitting.

4.4 Evaluation metrics for classification

The most common metrics for evaluating classification performance are the precision, recall, and F1-Score, which follow the standard definitions:

$$\text{precision} = \frac{tp}{tp + fp}, \quad (9)$$

$$\text{recall/true positive rate} = \frac{tp}{tp + fn}, \quad (10)$$

$$\text{false positive rate} = \frac{fp}{fp + tn}, \quad (11)$$

where tp , tn , fp , and fn are the true positive, true negative, false positive, and false negative values, respectively. The f1-score is defined as the harmonic mean of the precision and recall:

$$f1 = \frac{2 \times \text{precision} \times \text{recall}}{\text{precision} + \text{recall}} = \frac{2tp}{2tp + fp + fn}. \quad (12)$$

Besides these metrics, we also used the area under the curve AUC-ROC metric values for evaluation [48]. The AUC-ROC value was computed by integrating over the receiver operating characteristic (ROC) curve, plotting the true positive rate against the false positive rate.

4.5 Evaluation metrics for the explainability methods

An intuitive way to assess the quality of an explanation is by measuring its ability to accurately capture how the predictor function reacts to significant perturbations [49]. The feature importance scores from g should correspond to the important features of x for f ; as such, when we set particular features x_s to a baseline value x_s^f , the change in predictor's output should be proportional to the sum of attribution scores of features in x_s . We measure this as the correlation between the sum of the attributions of x_s and the difference in output when setting those features to a reference baseline [50]. Thus we define the faithfulness of an explanation method g by:

$$M_{faith}(f, g : x) = \text{corr}_S\left(\sum_{i \in S} g(f, x)_i, f(x) - f(x[x_s = x_s^f])\right) \quad (13)$$

where S a subset of indices ($S \subseteq [1, 2, 3 \dots d]$) denoted by x_s sub-vector of an input x ($x = x_s \cup x_f$ and x_f the unchanged features of x image). The total number of the x_s sub-vectors which partition an image is d . We denote as x_s^f the changed pixel x_f the unchanged features of x image.

If for an explanation the g method uses all the d sub-vectors of an image x then it is a very high complexity method. It is important to compute the level of complexity as an efficient explanation has to be simple with low complexity [50]. If P_g is a valid probability distribution the $P_g(i)$ is the fractional contribution of feature x_i to the total magnitude of the attribution, where:

$$M_{comp_x}(f, g : x) = \sum_{(i \in [1 \dots d])} P_g(i) (\log(\frac{1}{P_g(i)})) \quad (14)$$

where:

$$P_g(i) = \frac{|g(f, x)_i|}{\sum_{j \in [d]} |g(f, x)_j|} \quad (15)$$

and

$$P_g = P_g(1), \dots, P_g(d) \quad (16)$$

In order to evaluate the two corresponding techniques for explainability, we employed the software developed by [51]. This software package is a comprehensive toolkit that collects, organizes, and provides explanations for a wide range of evaluation metrics proposed for explanation methods. For this particular study, we utilized our network's predictions and explanations for 21 randomly chosen individuals from the testing group, and evaluated the faithfulness and complexity scores for explainability. The chosen hyperparameters included a zero perturbation baseline ('black'), a Pearson correlation similarity function, and 50 simulations for the Faithfulness score.

4.6 Data availability

This study used the datasets of the TOP-OSLO [17] which can be obtained from University of Oslo upon request, subject to a data transfer agreement.

4.7 Code availability

The code developed in this study is written in the Python programming language using Keras/TensorFlow (Python) libraries. For training and testing of deep learning networks, we have used an NVIDIA cluster with 4 GPUs and 64 GB RAM memory. The code is publicly available in <https://github.com/ece7048/3Dsulci>.

5 Results and Discussion

5.1 Classifiers performance for presence or absence of paracingulate sulcus

For brevity, we emphasized the simple-3D-MHL network out of the two backbones of the two-head attention layer network, as the performance of simple-3D-MHL, a deeper CNN by design, outperformed the two-level CNN backbone network (2CNN-3D-MHL). The results for 2CNN-3D-MHL can be found in the supplementary material, subsection 4.1, while the outcomes for the simple-3D-MHL and simple-3D-CNN networks are discussed in this section. Supplementary Extended DATA Fig. 1 shows the classification results of the simple-3D-MHL and simple-3D-CNN. The performance of the simple-3D-MHL network (Supplementary Extended DATA Fig. 1a.) in the left hemisphere (around 73.00% in all testing metrics and 74.10% in all validation metrics) was higher than that in the right hemisphere (around 58.00% in all testing metrics and 63.10% in the validation metrics). For the simple-3D-CNN (Supplementary Extended DATA Fig. 1b.), the performance of the network in the left hemisphere (around 72.90% in all testing metrics and 74.00% in all validation metrics) was higher than that in the right hemisphere (around 56.00% in all testing metrics and 63.00% in the validation metrics). This discrepancy in performance between the left and right hemisphere was to be expected for two reasons. First, the paracingulate sulcus is more prominent in the left than in the right hemisphere [52, 53], including in psychopathological situations such as schizophrenia [13], implying that the pattern recognition problem is better defined on the left hemisphere. Moreover, the left paracingulate sulcus shows more associations with regional cortical thickness and sulcal depth than the right one [12], implying more covariability of anatomical features contained in either of our input modalities with the presence of the paracingulate sulcus in the left hemisphere than in the right one.

5.2 Global explainability methods and their PCA component results

In this study, we extracted and evaluated the explainable results of both networks to avoid any biased observation, to study if there is a clear cause-and-effect relationship between the quality of explanation and the prediction of performance. Hence, the best explanation would lead to the best prediction performance.

The explainability results of simple-3D-MHL and simple-3D-CNN networks on the left and right hemisphere of the grey/white surface inputs show significant focus on the medial surface of the frontal lobe, thalamus and cingulate gyrus for detecting the presence of the paracingulate sulcus (PCS). Conversely, the absence of paracingulate sulcus (nPCS) is primarily detected by focusing on the thalamus and the anterior frontal lobe. In the left hemisphere significant focusing occurs on the thalamus following by the anterior front lobe. In the

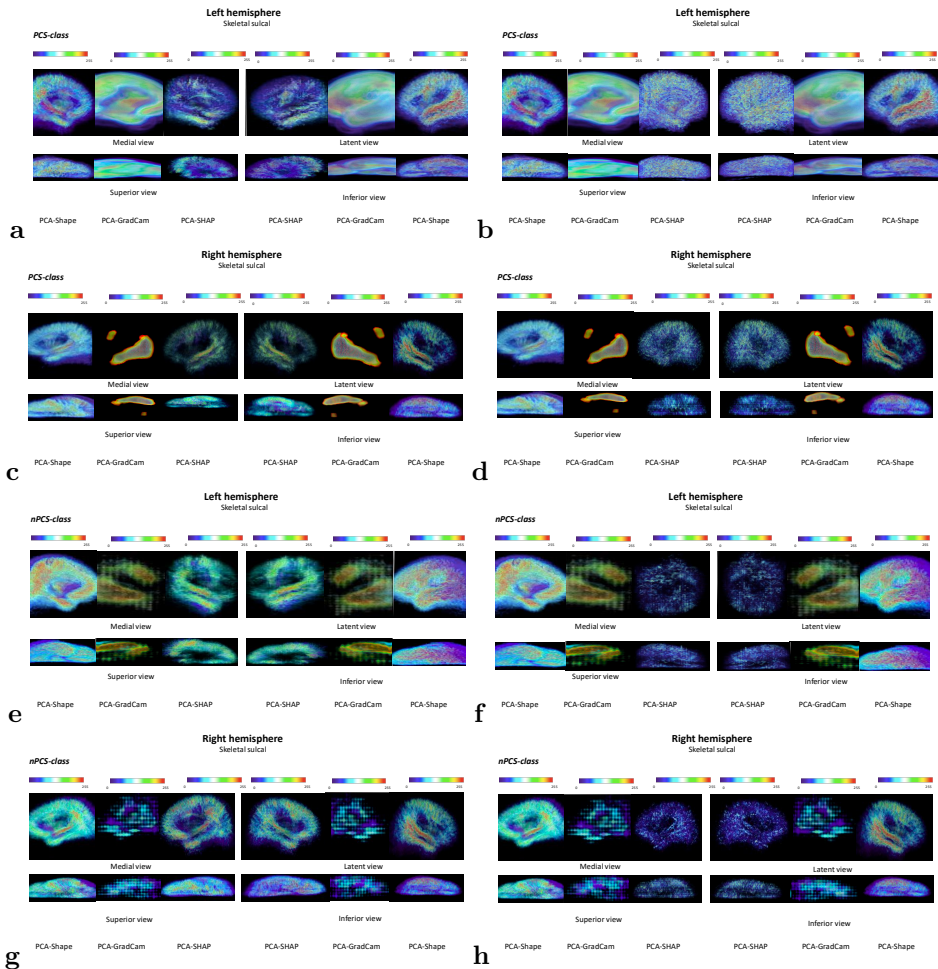
right hemisphere the region of significant focus is the thalamus and the anterior front lobe, following by the cingulate gyrus in some cases (PCA-Shape) (refer to Supplementary Extended DATA Fig. 2).

The explainability results of the deep learning networks on the left and right hemisphere of the sulcal skeleton brain inputs are presented in Fig. 5. For completeness, we also show the corresponding cases for PCA-Shape and PCA-GradCam, as well as PCA-Shape and PCA-SHAP, for both the left and right hemispheres of the skeletal sulcal input. The PCA-GradCam results from both the simple-3D-CNN and simple-3D-MHL models are nearly indistinguishable because Gradcam utilizes the same convolutional layer from these networks, and up to this stage, the structure of the two networks remains identical. Concerning the sulcal skeleton inputs on the left and right sides, Fig. 5.a,b display the comprehensive explanations of PCA-GradCam, PCA-SHAP, and PCA-Shape for both networks. The neural networks distinctly emphasize key regions in both hemispheres. In the left hemisphere, there's notable focus on superior temporal sulcus, insula, and inferior central and precentral sulci for the PCS class (Fig. 5a-b). Conversely, in the right hemisphere for the same class, emphasis is on superior temporal sulcus, collateral fissure, calcarine fissure, parieto-occipital fissure, and sub-parietal sulcus (Fig. 5c-d). For the nPCS class, the left hemisphere highlights specific areas, including superior temporal sulcus, insula, and inferior central and precentral sulci (Fig. 5e,f). In the right hemisphere, the focus shifts to superior temporal sulcus, inferior central sulcus, internal parietal sulcus, and anterior cingulate sulcus (Fig. 5g,h).

To validate the paracingulate sulcus presence or absence pattern, we assessed the variability across all six components of the PCA by visualizing the outcomes of PCA-Shape and PCA-GradCam for both hemispheres. Notably, we observed differences within the six PCA components in the explainability approach (PCA-GradCam) and the statistical features approach (PCA-Shape) (refer to Supplementary Extended DATA Fig. 3). We noticed differences in the intensity and extent of regions highlighted between sulcal skeleton and grey/white surface inputs, while the primary regions of focus remained consistent. To take this into account, we used the post-fusion mathematical formulation, of Eq. 8 to amalgamate all PCA components. This produced a global PCA representation of PCA-Shape, PCA-GradCam, and PCA-SHAP outputs, for both input modalities and both hemispheres separately.

Fig. 6a, provides a summary of the evaluation metrics, specifically faithfulness and complexity scores, for the SHAP and GradCam methods applied to the simple-3D-CNN and simple-3D-MHL networks. The results in Fig. 6a, demonstrate that SHAP generally outperforms GradCam in explaining the different inputs in both higher faithfulness and lower complexity of the local explanations.

Fig. 5: Simple-3D-MHL and simple-3D-CNN explainability results on the left and right hemisphere of sulcal skeleton brain inputs.



a-d, show the explainability results for the PCS class images of the first component among the six components of PCA for the total input modality (PCA-Shape), the total corresponding GradCam results (PCA-GradCam), and the total corresponding SHAP results (PCA-SHAP). The sub-figures **e-h**, show the explainability results for the nPCS class images of the first component among the six components of PCA for the total input modality (PCA-Shape), the total corresponding GradCam (PCA-GradCam), and the total corresponding SHAP results (PCA-SHAP). **a,c,e,g**, the left and right sulcal skeleton input images results for the simple-3D-MHL network. **b,d,f,h**, the left and right sulcal skeleton input results for the simple-3D-CNN network. The feature's importance (pixel attribution) varies from 0 (blue color) to 255 (red color), with high importance being 255 for the PCA-GradCam and PCA-Shape results and from -255 (blue color) to 255 (red color) for PCA-SHAP results. The -255 value indicates negative attribution. The orientation of the results are based on the medial, lateral, superior and inferior anatomical views.

5.3 Total overlapping pattern learning results using grey/white surface inputs

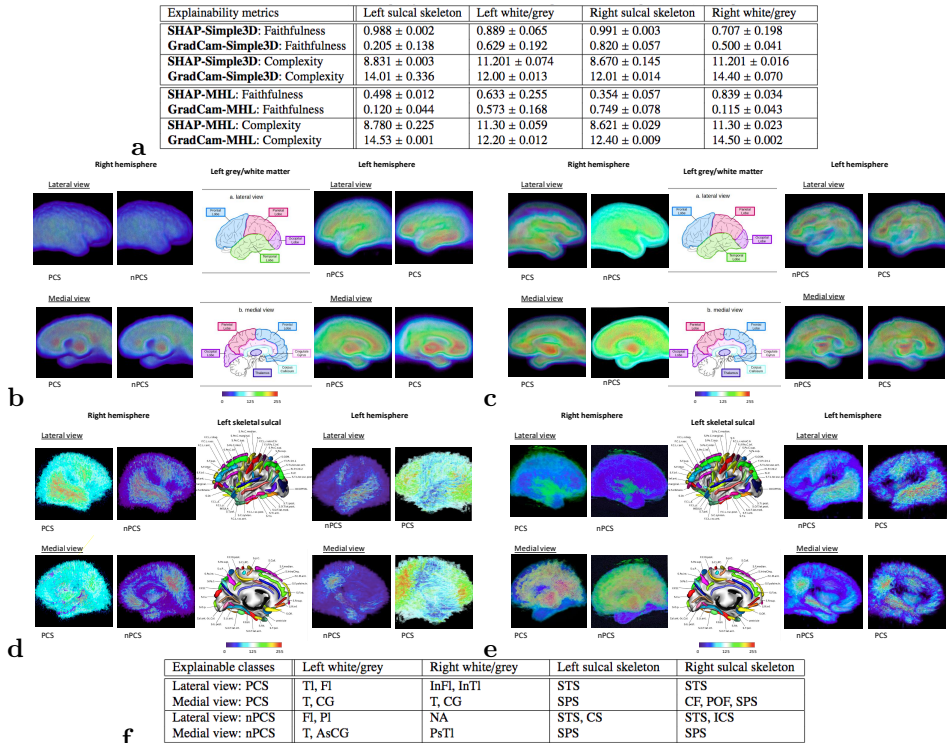
Based on the overlapping mathematical formulation of eq. 8 we extracted the global PCA pattern learning of both networks, by combining the PCA components of the PCA-SHAP, PCA-GradCam explanations (six weighted tensors) and the PCA-Shape statistical features to visualize the main explainability features. We then combined the three global PCA pattern learning results (PCA-SHAP, PCA-GradCam, PCA-Shape) by using the eq. 8 and the three weighted tensors to extract the total overlapping pattern learning results for each network (Fig. 6).

For the simple-3D-MHL on grey/white surface inputs (Fig. 6b.), the right hemisphere shows focus on the medial view, in the thalamus and cingulate gyrus both in the PCS and - to a lesser extent - in the nPCS conditions. The left hemisphere, shows different focuses based on the PCS and nPCS conditions. The PCS decision mostly relies on the inferior temporal lobe and anterior inferior frontal lobe in the lateral view, and on the thalamus, both the anterior and posterior parts of the cingulate gyrus, the anterior frontal lobe, and the temporal lobe in the medial view. The nPCS condition, on the other hand, shows predominant focus on the inferior prefrontal lobe, and the temporal lobe in the lateral view, and on the thalamus and cingulate gyrus in the medial view.

For the simple-3D-CNN on grey/white surface inputs (Fig. 6c.), in the right hemisphere, PCS condition, the highlights in the lateral view are in the inferior frontal lobe and inferior temporal lobe in the PCS condition, and those in the medial view are in the thalamus, cingulate gyrus, anterior occipital lobe, and posterior temporal lobe. Still on the right hemisphere, in the nPCS condition, the focus is on the medial view in the thalamus, the cingulate gyrus, the frontal lobe, and the posterior temporal lobe. In the left hemisphere, both conditions globally focus on the same regions, laterally in the middle frontal lobe, and inferior and superior parietal lobe, and medially in the thalamus and in the cingulate, frontal and parietal lobes, with a special focus on the anterior cingulate gyrus. The PCS condition additionally focuses on the lateral view of the posterior temporal lobe.

For both networks, in right hemisphere, the focus is essentially on the medial view (except for the PCS condition in the right hemisphere), with the main contributions in the thalamus and cingulate gyrus, suggesting a rather local explainability of the paracingulate sulcus's presence. Conversely, on the left hemisphere, the focus is much more globally distributed, with strong contributions stemming from the lateral view, suggesting that the developmental mechanisms leading to the presence of the paracingulate sulcus affect the brain at a larger scale [12].

Fig. 6: Explainable methods scores and the extraction of the total overlapping pattern learning explanation of the left and right hemisphere and different inputs with expert’s observation.



a Table with Evaluation of the faithfulness, and complexity of the SHAP and GradCam explanations in the simple-3D-CNN, and simple-3D-MHL. **b** shows the total overlapping pattern learning results for the right and left hemisphere of the brain for grey/white surface images of the simple-3D-MHL network. The sub-figure **c** shows the total overlapping pattern learning results for the right and left hemisphere of the brain grey/white surface images for of the simple-3D-CNN network. **d** shows the total overlapping pattern learning results for the right and left hemisphere of the brain for sulcal skeleton inputs of the simple-3D-MHL network. **e** shows the total overlapping pattern learning results for the right and left hemisphere of the brain for sulcal skeleton inputs of the simple-3D-CNN network. **f** shows the pattern learning results from the overlapping of the two deep learning networks (simple-3D-MHL, simple-3D-CNN), on the total overlapping pattern learning results of the lateral and medial view, based on experts’ observation. For the grey/white surface input we used the acronyms, Is: inferior surface, As: anterior surface, Ps: posterior surface, T: thalamus, H: hypothalamus, Fl: Frontal lobe, Ol: occipital lobe, TI: temporal lobe, Pl: parietal lobe, Cc: corpus callosum, CG: cingulate gyrus. For the skeleton sulcal input we used the acronyms, STS: superior temporal sulcus, CF: calcarine fissure, POF: parieto-occipital fissure, SPS: sub-parietal sulcus, ICS: inferior central sulcus, CS: central sulcus, NA: none.

5.4 Total overlapping pattern learning results using sulcal skeleton inputs

A consistent method to overlay the outputs of the sulcal skeleton similar to the process described for the grey/white surface outputs was applied. For the simple-3D-MHL on sulcal skeleton inputs (Fig. 6d.), in the right hemisphere, the PCS and nPCS show similar trends, with lateral focuses on the superior temporal sulcus and the inferior precentral sulcus, and medial focuses on the interior parietal sulcus, the sub-parietal sulcus and both the inferior and superior rostral sulci (dimmed in the PCS condition). In the left hemisphere, the PCS and nPCS conditions show very different highlights. In the PCS condition, the main lateral focuses are in the posterior part of the inferior temporal sulcus, the occipital sulcus and the inferior frontal sulcus, and the medial focuses are in the rostral sulci (superior and inferior) and in the parietal sulci (interior, sub-parietal and temporo-occipital fissure). In the nPCS condition, the main contributions are in the superior temporal sulcus and precentral sulcus in the lateral view, and in the sub-parietal sulcus in the medial view.

For the simple-3D-CNN on sulcal skeleton inputs (Fig. 6e.) both the right and the left hemispheres show similar trends in the PCS and nPCS conditions. In the right hemisphere, the lateral view is negligible compared to the medial view, where the main focus is on the callosal and parieto-occipital fissures and on the insula. In the left hemisphere, the main focus is found laterally in the superior temporal sulcus and medially in the collateral fissure and in the sub-parietal sulcus.

We thereafter identified the common regions between the two networks' outputs and summarized them within Fig. 6f. Specifically, for the accurate detection of PCS within the skeleton sulcal hemisphere inputs, the pivotal sub-regions encompass the superior temporal sulcus, inferior precentral sulcus, calcarine fissure, parieto-occipital fissure, and sub-parietal sulcus. Conversely, when PCS is absent, the critical sub-regions within the right hemisphere skeleton sulcal hemisphere inputs encompass the superior temporal sulcus, inferior central sulcus, and sub-parietal sulcus (Fig. 6f). Transitioning to the left hemisphere, the skeleton sulcal hemisphere inputs underscore the significance of the superior temporal sulcus and sub-parietal sulcus. When PCS is not present, the important left hemisphere sulcal skeleton inputs comprise the superior temporal sulcus, inferior and central sulcus (Fig. 6f).

We went one step further exploring the sulcal skeleton output of the simple-3D-MHL network as it slightly outperformed the simple-3D-CNN in the classification task. We applied an affine registration to the total overlapping results of sulcal skeleton inputs from each hemisphere onto a probabilistic atlas of sulci [54]. Fig. 7 illustrates the distribution of the most relevant voxels for outcome decision within sulcal probabilistic areas according to different thresholds. The decisions on the right hemisphere were highly focused on specific sulci, with up to three sulci contributing to the 20% threshold, which we retained as the lower threshold (blue). Conversely, the left hemisphere predictions were based on broader considerations, with a number of sulci already

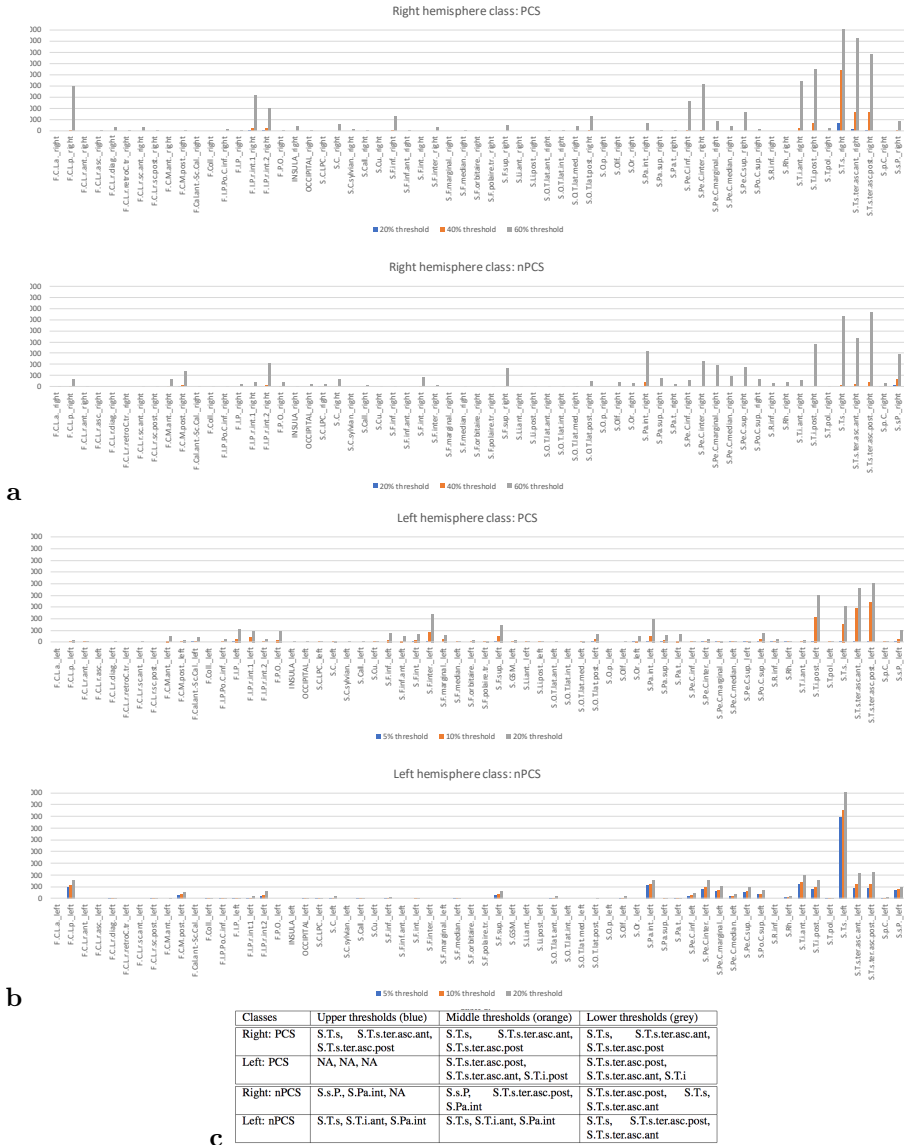
contributing to the decision based on the 5% threshold, which we retained as the lower threshold for the left hemisphere (blue). For both conditions and both hemisphere, a specific focus is set on the superior temporal sulcus and its posterior branches, and a smaller but consistent contribution of the internal parietal and sub-parietal sulci. The nPCS condition on the left hemisphere additionally focuses on the precentral sulcus and the Sylvian fissure. Interestingly, no specific focus is oriented towards the internal frontal sulcus (S.F.int), the probabilistic region in which the paracingulate sulcus is located when present.

5.5 Contrasting our 3D explainability framework outputs in a second dataset with a biased annotation protocol

In this study, we offered a valid annotation protocol and an unbiased validation procedure with the AI framework we proposed, specifically our novel 3D explainability framework. Our exploration was centered around a meticulously curated dataset (TOP-OSLO), labelled according to a strict annotation protocol designed by two expert neuroscientists. In the Supplementary materials of our manuscript we studied the application of the same 3D explainability framework to a second dataset (we will denote it as DATASET-B), annotated by an untrained scientist, and grossly dichotomized based on the presence of any paracingulate-compatible sulcus element, even small or sparse. We presented the classification outcomes derived from the simple-3D-CNN trained with DATASET-B, focusing on the left and right hemispheres of the brain. Notably, the network significantly outperformed in the left hemisphere compared to the right hemisphere. Metrics indicated a strikingly higher performance level of approximately 90% for the left hemisphere, against an approximate 71% for the right hemisphere (refer to supplementary Fig. 3). The classification outcomes derived from the simple-3D-MHL network underscored performance of about 80% across all metrics for the left hemisphere. This achievement significantly overshadowed the right hemisphere's performance, standing at around 70% (see supplementary Fig. 4).

A striking pattern emerged when analyzing the comparative performance of the simple-3D network and the MHL networks, especially within the context of DATASET-B. Notably, the MHL networks are overshadowed by the superiority of the simple-3D network. Interestingly, the dynamic shifts in performance were mirrored in TOP-OSLO dataset we presented in the main manuscript, as the MHL network outperformed the CNN and aided in augmenting generalization capabilities. These disparities could be attributed to the differential annotation protocols applied to the two datasets. Specifically, the bias introduced by the reliance on a single rater characterizes DATASET-B, while TOP-OSLO is characterized by impartiality, drawing from inputs by two senior experts following a strict protocol. This disparity highlights the paramount importance of meticulous dataset curation when deploying complex explainability frameworks.

Fig. 7: A representation depicting the presence and absence patterns of the paracingulate sulcus on the left and right hemispheres of the brain's sulcal skeleton.



a, b, are the histograms of the number of voxels per sulcus based on the probabilistic mapping of sulci for both conditions (PCS and nPCS) and both hemispheres, using sulcal skeleton brain input images with the simple-3D-MHL network. The voxels are extracted after thresholding for highest explainability values, with thresholds of the highest 20, 40, and 60% intensity on the right hemisphere and highest 5, 10, and 20% intensity on the left hemisphere (high threshold: blue, medium threshold: orange, low threshold: grey). **c,** the total overlapping pattern learning results of the three most significant sulcal sub-region for the three different level of intensity thresholding. The acronyms for all sulci are defined in Supplementary Extended DATA Fig. 4.

Intriguingly, we also observed divergent outcomes when utilizing DATASET-B (supplementary material), particularly the near-systematic prevalence of the occipital region within explainability. This observation fades away when the same methodology is applied to the meticulously curated dataset of TOP-OSLO (main manuscript).

5.6 Contribution and objectives

Explainability is essential in medical image analysis, categorizing AI into self-explainable (intuitive tasks like segmentation and registration), semi-explainable (requiring localized explanations due to varied annotations), and non-explainable applications (with highly variable annotations, necessitating validation through XAI methods). In our study this categorization has been mathematically formalized to encompass a comprehensive range of explanation requirements. AI is pivotal in filling knowledge gaps, especially in non-established disease annotations. It facilitates the study of brain anatomy and automates MRI-based sulcal feature detection, enhancing our understanding of cognitive function and neurological disorders. In this study, we introduced a novel 3D explainability framework to validate and interpret the pattern learning of deep learning networks in a binary classification task of a highly non-explainable application in brain sulcal topology. We focused on the presence or absence of the paracingulate sulcus and employed two different 3D deep learning networks: a simple deep 3D convolution neural network and a two-head attention layer network. Our aim was to train and test these networks to predict the presence/absence of PCS using a clinical dataset, which was divided into training, validation, and testing sets. Our notable contribution lies in creating a comprehensive 3D explainable framework that merges 3D local explainability methods, GradCam and SHAP, and global explanation through a dimensionality reduction technique. This integration unveiled insights into learned network patterns and offered global explanations for the classifications. Our meticulously designed 3D explainable framework not only provides localized and global interpretations but also identifies significant sub-regions through post-fusion transformation of explanatory and statistical features.

Through our analysis using the proposed 3D framework, we developed a novel pattern learning method for detecting the presence or absence of highly variable sulcal patterns, specifically focusing on the paracingulate sulcus. We discovered significant associations between specific anatomical regions of the brain through grey-white surface and sulcal skeleton inputs, that were distinct in the presence or absence of PCS. These findings enhance our understanding of the neural mechanisms related to the developmental origins of the PCS and provide valuable insights for future research in the field of neurological and psychiatric disorders. The regions of focus, both stemming from the grey/white matter interface and sulcal skeleton inputs, call for a globalized reflection about the neurodevelopmental mechanisms leading to the formation of a paracingulate sulcus (or absence thereof). The focus, which is decentralized from the region of definition of the paracingulate sulcus, suggests that the most relevant

information about its presence of the paracingulate sulcus is located elsewhere, which is counter intuitive. Yet, this result may relay developmental insights regarding the mechanisms leading to the potential formation of the paracingulate sulcus [29]. When looking at the sulcal skeleton results, while the timing of apparition of the internal parietal and sub-parietal sulci are unreported, the superior temporal and prefrontal sulci are both reported to first appear around 26 weeks of gestational age in the fetus [55, 56], while the paracingulate sulcus (which would be part of the secondary cingulate folding) only starts to appear around 31 weeks of gestational age [55]. The relationship between those sulci could therefore indicate an earlier chronology of the events orchestrating the apparition of a paracingulate sulcus. This could hint towards a greater genetic constraint on this sulcus as earlier developing sulci have been reported to show more heritability [57]. Incidentally, the relevance of the Sylvian fissure in the results may imply an intertwining of gyrification and opercularization in the mechanisms leading to the formation of a paracingulate sulcus. This could be a potential explanation for the commonly reported leftward predominance of the left paracingulate sulcus, as, while gyrification shows a rightward developmental advance, opercularization has been reported to show a leftward advance [30]. Therefore, the concurrent intervention of these two phenomena could justify the asymmetrical patterning of the developing paracingulate sulcus and potentially its resulting form; in that case, the presence of this sulcus could be influenced by even earlier developmental events as opercularization starts before gyration and is importantly genetically regulated [58]

Moreover, this study investigated the significance of a valid annotation protocol and unbiased validation procedure in our proposed deep learning classifiers and 3D XAI framework. The emphasis has been on a carefully curated dataset (TOP-OSLO), compared to a second dataset (DATASET-B), annotated by an untrained scientist and presented in supplementary materials. The second dataset's divergent outcomes highlight the necessity for meticulous dataset curation. Our study introduces an automated and impartial annotation process, enhancing the possibilities for comprehensive explorations of sulcal development in relationship to cognitive and behavioral development. In the realm of deep learning and neuroscience, our contribution is a pioneering 3D explainable framework validating pattern learning in computer vision classifications tasks. Applied to paracingulate detection, our frameworks allowed to explore anatomical covariability and incidentally delve into the chronology of events intertwining structural and functional consequences.

5.7 Limitations and future work

The effectiveness of our framework remains dependent on the quality and diversity of accessible data, and its performance could differ in alternate contexts. Additionally, while the incorporation of explainability techniques contributes to interpretability, it might not encompass all underlying intricacies of network behavior. The selection of the two local methods necessitates further exploration of alternative approaches to ensure comprehensiveness. The

enhancement of classification outcomes demands the incorporation of additional information beyond structural MRI data to achieve improved accuracy. To further investigate and incorporate more intricate strategies, the combination of XAI techniques and PCA can explore overlapping aspects. Furthermore, complex approaches like t-SNE for non-linear dimensionality reduction can be employed to delve deeper into the subject. Moving forward, we envision expanding the framework's applicability to other neurological conditions and classification tasks (such as schizophrenia or bipolar disorder), employing external datasets like BeneMIN datasets [59], [60], and further refining the interpretability techniques. Our study paves the way for a more systematic exploration of sulcal variability through the lens of deep learning, which can help explore cognitive and functional variability as well as pathological changes.

6 Conclusion

In this study, we have introduced a mathematical formulation that categorizes different explanation requirements within diverse computer vision tasks, identifying them as: self-explainable, semi-explainable, non-explainable, and new-pattern learning. We have developed a 3D explainable framework designed to furnish both localized and comprehensive explanations, complemented by the outcomes of classification. Moreover, this framework has provided the means to pinpoint sub-regions crucial to decision-making via a post-fusion transformation of both explanatory and statistical features. Notably, our framework has revealed meaningful associations between brain sub-regions and the presence or absence of the paracingulate sulcus, thereby deepening our grasp of the underlying developmental mechanisms. Additionally, our study has underscored the pivotal importance of reliable annotation protocols and unbiased validation within our AI framework. By contrasting our outcomes with those derived from a subset of subjects marked by less dependable annotations, we have underscored the substantial impact on performance, underscoring the imperative of meticulous data curation. This endeavor advances the realms of both deep learning and neuroscience, enabling automated and impartial annotations while illuminating intricate neuroanatomical relationships across diverse subregions. Our 3D explainability framework offers unparalleled insights, thus setting the stage for comprehensive exploration within the ever-evolving domains of deep learning and neuroscience.

Supplementary information. The manuscript contains supplementary material.

References

- [1] Mamalakis, A., Ebert-Uphoff, I., Barnes, E.A.: Neural network attribution methods for problems in geoscience: A novel synthetic benchmark dataset.

- Environmental Data Science **1**, 8 (2022). <https://doi.org/10.1017/eds.2022.7>
- [2] Ghosh, S., Pal, A., Jaiswal, S., Santosh, K.C., Das, N., Nasipuri, M.: Segfast-v2: Semantic image segmentation with less parameters in deep learning for autonomous driving. *International Journal of Machine Learning and Cybernetics* **10**(11), 3145–3154 (2019). <https://doi.org/10.1007/s13042-019-01005-5>
- [3] Yu, X., Zuo, Y., Wang, Z., Zhang, X., Zhao, J., Yang, Y., Jiao, L., Peng, R., Wang, X., Zhang, J., Zhang, K., Liu, F., Alcover-Couso, R., San-Miguel, J.C., Escudero-Viñolo, M., Tian, H., Matsui, K., Wang, T., Adan, F., Gao, Z., He, X., Bouniot, Q., Moghaddam, H., Rai, S.N., Cermelli, F., Masone, C., Pilzer, A., Ricci, E., Bursuc, A., Solin, A., Trapp, M., Li, R., Yao, A., Chen, W., Simpson, I., Campbell, N.D.F., Franchi, G.: The Robust Semantic Segmentation UNCV2023 Challenge Results (2023)
- [4] Mamalakis, M., Garg, P., Nelson, T., Lee, J., Swift, A.J., Wild, J.M., Clayton, R.H.: Automatic development of 3d anatomical models of border zone and core scar regions in the left ventricle. *Computerized Medical Imaging and Graphics* **103**, 102152 (2023). <https://doi.org/10.1016/j.compmedimag.2022.102152>
- [5] Mamalakis, M., Macfarlane, S.C., Notley, S.V., Gad, A.K.B., Panoutsos, G.: A novel framework employing deep multi-attention channels network for the autonomous detection of metastasizing cells through fluorescence microscopy (2023)
- [6] Mamalakis, M., Garg, P., Nelson, T., Lee, J., Wild, J.M., Clayton, R.H.: Ma-socratis: An automatic pipeline for robust segmentation of the left ventricle and scar. *Computerized Medical Imaging and Graphics* **93**, 101982 (2021). <https://doi.org/10.1016/j.compmedimag.2021.101982>
- [7] Mamalakis, M., Garg, P., Nelson, T., Lee, J., Swift, A.J., Wild, J.M., Clayton, R.H.: Artificial intelligence framework with traditional computer vision and deep learning approaches for optimal automatic segmentation of left ventricle with scar. *Artificial Intelligence in Medicine* **143**, 102610 (2023). <https://doi.org/10.1016/j.artmed.2023.102610>
- [8] Mamalakis, M., Dwivedi, K., Sharkey, M., Alabed, S., Kiely, D., Swift, A.J.: A transparent artificial intelligence framework to assess lung disease in pulmonary hypertension. *Scientific Reports* **13**(1), 3812 (2023). <https://doi.org/10.1038/s41598-023-30503-4>
- [9] Cachia, A., Borst, G., Tissier, C., Fisher, C., Plaze, M., Gay, O., Rivière, D., Gogtay, N., Giedd, J., Mangin, J.-F., Houdé, O., Raznahan, A.: Longitudinal stability of the folding pattern of the anterior cingulate cortex

- during development **19**, 122–127. <https://doi.org/10.1016/j.dcn.2016.02.011>. Accessed 2021-12-17
- [10] Borne, L., Rivière, D., Mancip, M., Mangin, J.-F.: Automatic labeling of cortical sulci using patch- or CNN-based segmentation techniques combined with bottom-up geometric constraints **62**, 101651. <https://doi.org/10.1016/j.media.2020.101651>. Accessed 2020-03-17
- [11] Jiang, X., Zhang, T., Zhang, S., Kendrick, K.M., Liu, T.: Fundamental functional differences between gyri and sulci: implications for brain function, cognition, and behavior **1**(1), 23–41. <https://doi.org/10.1093/psyrad/kkab002>. Accessed 2021-12-17
- [12] Fornito, A., Yücel, M., Wood, S.J., Proffitt, T., McGorry, P.D., Velakoulis, D., Pantelis, C.: Morphology of the paracingulate sulcus and executive cognition in schizophrenia **88**(1), 192–197. <https://doi.org/10.1016/j.schres.2006.06.034>. Accessed 2022-09-08
- [13] Garrison, J.R., Fernyhough, C., McCarthy-Jones, S., Haggard, M., The Australian Schizophrenia Research Bank, Simons, J.S.: Paracingulate sulcus morphology is associated with hallucinations in the human brain **6**(1), 8956. <https://doi.org/10.1038/ncomms9956>. Accessed 2022-09-07
- [14] Gay, O., Plaze, M., Oppenheim, C., Gaillard, R., Olié, J.-P., Krebs, M.-O., Cachia, A.: Cognitive control deficit in patients with first-episode schizophrenia is associated with complex deviations of early brain development **42**(2), 87–94. <https://doi.org/10.1503/jpn.150267>. Accessed 2021-12-17
- [15] Ćurčić-Blake, B., de Vries, A., Renken, R.J., Marsman, J.B.C., Garrison, J., Hugdahl, K., Aleman, A.: Paracingulate sulcus length and cortical thickness in schizophrenia patients with and without a lifetime history of auditory hallucinations. *Schizophrenia Bulletin* **49**(Supplement_1), 48–57 (2023). <https://doi.org/10.1093/schbul/sbac072>
- [16] Simons, J.S., Garrison, J.R., Johnson, M.K.: Brain mechanisms of reality monitoring **21**(6), 462–473. <https://doi.org/10.1016/j.tics.2017.03.012>. Accessed 2021-12-16
- [17] Mørch-Johnsen, L., Nesvåg, R., Jørgensen, K.N., Lange, E.H., Hartberg, C.B., Haukvik, U.K., Kompus, K., Westerhausen, R., Osnes, K., Andreassen, O.A., Melle, I., Hugdahl, K., Agartz, I.: Auditory cortex characteristics in schizophrenia: Associations with auditory hallucinations **43**(1), 75–83. <https://doi.org/10.1093/schbul/sbw130>. Accessed 2023-07-20
- [18] Fedeli, D., Del Maschio, N., Caprioglio, C., Sulpizio, S., Abutalebi, J.:

- Sulcal pattern variability and dorsal anterior cingulate cortex functional connectivity across adult age **10**(6), 267–278. <https://doi.org/10.1089/brain.2020.0751>. Accessed 2022-10-04
- [19] Rollins, C.P.E., Garrison, J.R., Arribas, M., Seyedsalehi, A., Li, Z., Chan, R.C.K., Yang, J., Wang, D., Liò, P., Yan, C., Yi, Z.-h., Cachia, A., Uptegrove, R., Deakin, B., Simons, J.S., Murray, G.K., Suckling, J.: Evidence in cortical folding patterns for prenatal predispositions to hallucinations in schizophrenia **10**(1), 387. <https://doi.org/10.1038/s41398-020-01075-y>. Accessed 2021-12-28
- [20] Mangin, J.-F., Perrot, M., Operto, G., Cachia, A., Fischer, C., Lefèvre, J., Rivière, D.: Sulcus identification and labeling. In: Brain Mapping, pp. 365–371. Elsevier. <https://doi.org/10.1016/B978-0-12-397025-1.00307-9>. <https://linkinghub.elsevier.com/retrieve/pii/B9780123970251003079>. Accessed 2020-02-28
- [21] Yang, J., Wang, D., Rollins, C., Leming, M., Liò, P., Suckling, J., Murray, G., Garrison, J., Cachia, A.: Volumetric segmentation and characterisation of the paracingulate sulcus on MRI scans. <https://doi.org/10.1101/859496>. Accessed 2021-12-17
- [22] Cointepas, Y., Mangin, J.-F., Garnero, L., Poline, J.-B., Benali, H.: Brainvisa: Software platform for visualization and analysis of multi-modality brain data. *NeuroImage* **13**(6, Supplement), 98 (2001). [https://doi.org/10.1016/S1053-8119\(01\)91441-7](https://doi.org/10.1016/S1053-8119(01)91441-7). Originally published as Volume 13, Number 6, Part 2
- [23] Mangin, J.-F., Rivière, D., Duchesnay, E., Cointepas, Y., Gaura, V., Verny, C., Damier, P., Krystkowiak, P., Bachoud-Lévi, A.-C., Hantraye, P., Remy, P., Douaud, G.: Neocortical morphometry in huntington’s disease: Indication of the coexistence of abnormal neurodevelopmental and neurodegenerative processes **26**, 102211. <https://doi.org/10.1016/j.nicl.2020.102211>. Accessed 2021-05-03
- [24] Cachia, A., Paillère-Martinot, M.-L., Galinowski, A., Januel, D., de Beaurepaire, R., Bellivier, F., Artiges, E., Andoh, J., Bartrés-Faz, D., Duchesnay, E., Rivière, D., Plaze, M., Mangin, J.-F., Martinot, J.-L.: Cortical folding abnormalities in schizophrenia patients with resistant auditory hallucinations **39**(3), 927–935. <https://doi.org/10.1016/j.neuroimage.2007.08.049>. Accessed 2020-10-28
- [25] Plaze, M., Paillere-Martinot, M.-L., Penttila, J., Januel, D., de Beaurepaire, R., Bellivier, F., Andoh, J., Galinowski, A., Gallarda, T., Artiges, E., Olie, J.-P., Mangin, J.-F., Martinot, J.-L., Cachia, A.: ”where do auditory hallucinations come from?”—a brain morphometry study of schizophrenia patients with inner or outer space hallucinations **37**(1),

- 212–221. <https://doi.org/10.1093/schbul/sbp081>. Accessed 2020-11-03
- [26] Coulon, O., Lefevre, J., Kloppel, S., Siebner, H., Mangin, J.-F.: Quasi-isometric length parameterization of cortical sulci: Application to handedness and the central sulcus morphology. In: 2015 IEEE 12th International Symposium on Biomedical Imaging (ISBI), pp. 1268–1271. IEEE. <https://doi.org/10.1109/ISBI.2015.7164105>. <http://ieeexplore.ieee.org/document/7164105/> Accessed 2021-07-26
- [27] Leroy, F., Cai, Q., Bogart, S.L., Dubois, J., Coulon, O., Monzalvo, K., Fischer, C., Glasel, H., Van der Haegen, L., Bénézit, A., Lin, C.-P., Kennedy, D.N., Ihara, A.S., Hertz-Pannier, L., Moutard, M.-L., Poupon, C., Brysbaert, M., Roberts, N., Hopkins, W.D., Mangin, J.-F., Dehaene-Lambertz, G.: New human-specific brain landmark: The depth asymmetry of superior temporal sulcus **112**(4), 1208–1213. <https://doi.org/10.1073/pnas.1412389112>. Accessed 2021-02-23
- [28] Sun, Z.Y., Pinel, P., Rivière, D., Moreno, A., Dehaene, S., Mangin, J.-F.: Linking morphological and functional variability in hand movement and silent reading **221**(7), 3361–3371. <https://doi.org/10.1007/s00429-015-1106-8>. Accessed 2020-01-14
- [29] De Vareilles, H., Rivière, D., Pascucci, M., Sun, Z.-Y., Fischer, C., Leroy, F., Tataranno, M.-L., Benders, M.J., Dubois, J., Mangin, J.-F.: Exploring the emergence of morphological asymmetries around the brain’s sylvian fissure: a longitudinal study of shape variability in preterm infants. *Cerebral Cortex* **33**(11), 6667–6680 (2023) <https://arxiv.org/abs/https://academic.oup.com/cercor/article-pdf/33/11/6667/50433767/bhac533.pdf>. <https://doi.org/10.1093/cercor/bhac533>
- [30] de Vareilles, H., Rivière, D., Mangin, J., Dubois, J.: Development of cortical folds in the human brain: An attempt to review biological hypotheses, early neuroimaging investigations and functional correlates **61**, 101249. <https://doi.org/10.1016/j.dcn.2023.101249>. Accessed 2023-06-01
- [31] Meng, Y., Li, G., Wang, L., Lin, W., Gilmore, J.H., Shen, D.: Discovering cortical sulcal folding patterns in neonates using large-scale dataset **39**(9), 3625–3635. <https://doi.org/10.1002/hbm.24199>. Accessed 2020-01-13
- [32] Samek, W., Montavon, G., Lapuschkin, S., Anders, C.J., Müller, K.-R.: Explaining deep neural networks and beyond: A review of methods and applications. *Proceedings of the IEEE* **109**(3), 247–278 (2021). <https://doi.org/10.1109/JPROC.2021.3060483>
- [33] van der Velden, B.H.M., Kuijff, H.J., Gilhuijs, K.G.A., Viergever, M.A.: Explainable artificial intelligence (xai) in deep learning-based medical

- image analysis. *Medical Image Analysis* **79**, 102470 (2022). <https://doi.org/10.1016/j.media.2022.102470>
- [34] Quellec, G., Al Hajj, H., Lamard, M., Conze, P.-H., Massin, P., Cochener, B.: Explain: Explanatory artificial intelligence for diabetic retinopathy diagnosis. *Medical Image Analysis* **72**, 102118 (2021). <https://doi.org/10.1016/j.media.2021.102118>
- [35] van der Velden, B.H.M.: Explainable ai: current status and future potential. *European Radiology* (2023). <https://doi.org/10.1007/s00330-023-10121-4>
- [36] Singh, A., Sengupta, S., Lakshminarayanan, V.: Explainable deep learning models in medical image analysis (2020)
- [37] Bach, S., Binder, A., Montavon, G., Klauschen, F., Müller, K.-R., Samek, W.: On pixel-wise explanations for non-linear classifier decisions by layer-wise relevance propagation. *PLOS ONE* **10**(7), 1–46 (2015). <https://doi.org/10.1371/journal.pone.0130140>
- [38] Rajani, N.F., McCann, B., Xiong, C., Socher, R.: Explain Yourself! Leveraging Language Models for Commonsense Reasoning (2019)
- [39] Tjoa, E., Guan, C.: A survey on explainable artificial intelligence (xai): Toward medical xai. *IEEE Transactions on Neural Networks and Learning Systems*, 1–21 (2020). <https://doi.org/10.1109/tnnls.2020.3027314>
- [40] Fellous, J.-M., Sapiro, G., Rossi, A., Mayberg, H., Ferrante, M.: Explainable artificial intelligence for neuroscience: Behavioral neurostimulation. *Frontiers in Neuroscience* **13** (2019). <https://doi.org/10.3389/fnins.2019.01346>
- [41] Vaswani, A., Shazeer, N., Parmar, N., Uszkoreit, J., Jones, L., Gomez, A.N., Kaiser, L.u., Polosukhin, I.: Attention is all you need. In: Guyon, I., Luxburg, U.V., Bengio, S., Wallach, H., Fergus, R., Vishwanathan, S., Garnett, R. (eds.) *Advances in Neural Information Processing Systems*, vol. 30. Curran Associates, Inc., ??? (2017)
- [42] Lundberg, S., Lee, S.-I.: A Unified Approach to Interpreting Model Predictions. *arXiv* (2017). <https://doi.org/10.48550/ARXIV.1705.07874>. <https://arxiv.org/abs/1705.07874>
- [43] Mitchell, S.C., De Vareilles, H., Garrison, J.R., Al-Manea, A., Suckling, J., Murray, G.K., Simons, J.S.: Paracingulate sulcus measurement protocol v2 (2023). <https://doi.org/10.17863/CAM.102040>
- [44] Vonesch, C., Unser, M.: A fast thresholded landweber algorithm for

- wavelet-regularized multidimensional deconvolution. *IEEE Transactions on Image Processing* **17**(4), 539–549 (2008)
- [45] Perona, P., Malik, J.: Scale-space and edge detection using anisotropic diffusion. *IEEE Transactions on Pattern Analysis and Machine Intelligence* **12**(7), 629–639 (1990)
- [46] Rivière, D., Mangin, J.-F., Papadopoulos-Orfanos, D., Martinez, J.-M., Frouin, V., Régis, J.: Automatic recognition of cortical sulci of the human brain using a congregation of neural networks **6**(2), 77–92. [https://doi.org/10.1016/S1361-8415\(02\)00052-X](https://doi.org/10.1016/S1361-8415(02)00052-X). Accessed 2021-05-03
- [47] Kingma, D.P., Ba, J.: Adam: A Method for Stochastic Optimization. arXiv (2014). <https://doi.org/10.48550/ARXIV.1412.6980>. <https://arxiv.org/abs/1412.6980>
- [48] Davis, J., Goadrich, M.: The relationship between precision-recall and roc curves. In: *Proceedings of the 23rd International Conference on Machine Learning*, pp. 233–240 (2006)
- [49] Yeh, C.-K., Hsieh, C.-Y., Suggala, A.S., Inouye, D.I., Ravikumar, P.: On the (in)fidelity and sensitivity for explanations (2019). <https://doi.org/10.48550/ARXIV.1901.09392>
- [50] Bhatt, U., Weller, A., Moura, J.M.F.: Evaluating and aggregating feature-based model explanations (2020). <https://doi.org/10.48550/ARXIV.2005.00631>
- [51] Hedström, A., Weber, L., Krakowczyk, D., Bareeva, D., Motzkus, F., Samek, W., Lapuschkin, S., Höhne, M.M.M.-: Quantus: An explainable ai toolkit for responsible evaluation of neural network explanations and beyond. *Journal of Machine Learning Research* **24**(34), 1–11 (2023)
- [52] Paus, T., Tomaiuolo, F., Otaky, N., MacDonald, D., Petrides, M., Atlas, J., Morris, R., Evans, A.C.: Human cingulate and paracingulate sulci: Pattern, variability, asymmetry, and probabilistic map **6**(2), 207–214. <https://doi.org/10.1093/cercor/6.2.207>. Accessed 2022-01-14
- [53] Yücel, M., Stuart, G.W., Maruff, P., Velakoulis, D., Crowe, S.F., Savage, G., Pantelis, C.: Hemispheric and Gender-related Differences in the Gross Morphology of the Anterior Cingulate/Paracingulate Cortex in Normal Volunteers: An MRI Morphometric Study. *Cerebral Cortex* **11**(1), 17–25 (2001) <https://arxiv.org/abs/https://academic.oup.com/cercor/article-pdf/11/1/17/9751090/1100017.pdf>. <https://doi.org/10.1093/cercor/11.1.17>

- [54] Perrot, M., Rivière, D., Mangin, J.-F.: Cortical sulci recognition and spatial normalization **15**(4), 529–550. <https://doi.org/10.1016/j.media.2011.02.008>. Accessed 2020-02-28
- [55] Garel, C., Chantrel, E., Brisse, H., Elmaleh, M., Luton, D., Oury, J.-F., Sebag, G., Hassan, M.: Fetal cerebral cortex: Normal gestational landmarks identified using prenatal mr imaging. *American Journal of Neuroradiology* **22**(1), 184–189 (2001) <https://arxiv.org/abs/https://www.ajnr.org/content/22/1/184.full.pdf>
- [56] Habas, P.A., Scott, J.A., Roosta, A., Rajagopalan, V., Kim, K., Rousseau, F., Barkovich, A.J., Glenn, O.A., Studholme, C.: Early folding patterns and asymmetries of the normal human brain detected from in utero MRI **22**(1), 13–25. <https://doi.org/10.1093/cercor/bhr053>. Accessed 2020-06-09
- [57] Pizzagalli, F., Auzias, G., Yang, Q., Mathias, S.R., Faskowitz, J., Boyd, J.D., Amini, A., Rivière, D., McMahon, K.L., de Zubicaray, G.I., Martin, N.G., Mangin, J.-F., Glahn, D.C., Blangero, J., Wright, M.J., Thompson, P.M., Kochunov, P., Jahanshad, N.: The reliability and heritability of cortical folds and their genetic correlations across hemispheres **3**(1), 510. <https://doi.org/10.1038/s42003-020-01163-1>. Accessed 2021-05-03
- [58] Mallela, A.N., Deng, H., Brisbin, A.K., Bush, A., Goldschmidt, E.: Sylvian fissure development is linked to differential genetic expression in the pre-folded brain **10**(1), 14489. <https://doi.org/10.1038/s41598-020-71535-4>. Accessed 2020-09-23
- [59] Lisiecka, D.M., Suckling, J., Barnes, T.R., Chaudhry, I.B., Dazzan, P., Husain, N., Jones, P.B., Joyce, E.M., Lawrie, S.M., Upthegrove, R., Deakin, B.: The benefit of minocycline on negative symptoms in early-phase psychosis in addition to standard care - extent and mechanism (benemin): study protocol for a randomised controlled trial. *Trials* **16**(1), 71 (2015). <https://doi.org/10.1186/s13063-015-0580-x>
- [60] Deakin, B., Suckling, J., Barnes, T.R.E., Byrne, K., Chaudhry, I.B., Dazzan, P., Drake, R.J., Giordano, A., Husain, N., Jones, P.B., Joyce, E., Knox, E., Krynicky, C., Lawrie, S.M., Lewis, S., Lisiecka-Ford, D.M., Nikkheslat, N., Pariante, C.M., Smallman, R., Watson, A., Williams, S.C.R., Upthegrove, R., Dunn, G.: The benefit of minocycline on negative symptoms of schizophrenia in patients with recent-onset psychosis (benemin): a randomised, double-blind, placebo-controlled trial. *The Lancet Psychiatry* **5**(11), 885–894 (2018). [https://doi.org/10.1016/S2215-0366\(18\)30345-6](https://doi.org/10.1016/S2215-0366(18)30345-6)

*

Acknowledgment All research at the Department of Psychiatry in the University of Cambridge is supported by the NIHR Cambridge Biomedical Research Centre (NIHR203312) and the NIHR Applied Research Collaboration East of England. The views expressed are those of the author(s) and not necessarily those of the NIHR or the Department of Health and Social Care. This study was supported by funding from the Medical Research Council, grant number: MR/W020025/1. We acknowledge the use of the facilities of the Research Computing Services (RCS) of University of Cambridge, UK. GKM consults for ieso digital health. All other authors declare that they have no competing interests.

*

Author information

*

Authors and Affiliations

Department of Psychiatry, University of Cambridge, Cambridge, UK.

Michail Mamalakis, Heloise de Vareilles, Atheer Al-Manea, John Suckling

Department of Computer Science and Technology, Computer Laboratory, University of Cambridge, Cambridge, UK.

Michail Mamalakis, Pietro Lio

Department of Psychology, University of Cambridge, Cambridge, UK.

Samantha C. Mitchell, Jane Garrison, Jon Simons

Department of Psychiatric Research, Diakonhjemmet Hospital, Oslo, Norway

Ingrid Agartz

Norment, Division of Mental Health and Addiction, Oslo University Hospital, Institute of Clinical Medicine, University of Oslo, Oslo, Norway.

Lynn Egeland Mørch-Johnsen

Department of Psychiatry and Department of Clinical Research, Østfold Hospital, Grålum, Norway.

Lynn Egeland Mørch-Johnsen

*

Contributions M.M, H.V., P.L., J.S. and G.M. conceived the study. M.M. wrote the code and conducted the experiments. I.A., LE.MJ., H.V., A.AM., and S.C.M. collected and pre-processed the data cohort. M.M, and H.V. analyzed the data and results. M.M. contributed to pulling deep learning and XAI methods and conducted chart reviews. M.M contributed to the experimental

design and validation protocol. G.M.,J.S.,P.L., H.V. and M.M. was in charge of overall direction and planning. All authors contributed to the interpretation of the results. M.M., H.V. and P.L. visualized the study and extracted figures, and M.M and H.V. drafted the manuscript, which was reviewed, revised and approved by all authors.

*

Corresponding author Correspondence to Michail Mamalakis or Graham Murray

*

Ethics declarations

Competing interests

The authors declare no competing interests.